Structure and mechanism of a novel cytomegaloviral DCAF mediating interferon antagonism

Vu Thuy Khanh Le-Trilling[1,9], Sofia Banchenko[2,9], Darius Paydar[1], Pia Madeleine Leipe[1], Lukas Binting[2], Simon Lauer[2], Andrea Graziadei[3], Christine Gotthold[2], Jörg Bürger[2,4], Thilo Bracht[5,6], Barbara Sitek[5,6], Robert Jan Lebbink[7], Anna Malyshkina[1], Thorsten Mielke[4], Juri Rappsilber[3,8], Christian M. T. Spahn[2], Sebastian Voigt[1,*], Mirko Trilling[1,*], David Schwefel[2,10,*]

[1] Institute for Virology, University Hospital Essen, University of Duisburg-Essen, Essen, Germany

[2] Charité – Universitätsmedizin Berlin, corporate member of Freie Universität Berlin and Humboldt-Universität zu Berlin, Institute of Medical Physics and Biophysics, Berlin, Germany

[3] Bioanalytics Unit, Institute of Biotechnology, Technische Universität Berlin, Berlin, Germany

[4] Microscopy and Cryo-Electron Microscopy Service Group, Max-Planck-Institute for Molecular Genetics, Berlin, Germany

[5] Medizinisches Proteom-Center, Ruhr-University Bochum, Bochum, Germany

[6] Department of Anesthesia, Intensive Care Medicine and Pain Therapy, University Hospital Knappschaftskrankenhaus Bochum, Bochum, Germany

[7] Department of Medical Microbiology, University Medical Center Utrecht, Utrecht, the Netherlands

[8] Wellcome Centre for Cell Biology, University of Edinburgh, Edinburgh, United Kingdom

[9] These authors contributed equally

[10] Lead contact

* Correspondence: sebastian.voigt@uk-essen.de (S.V.), mirko.trilling@uk-essen.de (M.T.), david.schwefel@charite.de (D.S.)

Abstract

Human cytomegalovirus (CMV) is a highly relevant pathogen, and its rodent counterparts serve as common infection models. Global proteome profiling of rat CMV-infected cells uncovered a pronounced loss of the transcription factor STAT2, which is crucial for interferon signalling. Deletion mutagenesis documented that STAT2 is targeted by the viral protein E27. Cellular and *in vitro* analyses showed that E27 exploits host-derived Cullin4-RING ubiquitin ligases (CRL4) to induce poly-ubiquitylation and proteasomal degradation of STAT2. Cryo-electron microscopic structure determination revealed how E27 mimics molecular surface properties of cellular CRL4 substrate receptors (DDB1- and Cullin4-associated factors, DCAFs) to displace them from the CRL4 catalytic core. Moreover, structural analyses elucidated the mechanism of STAT2 recruitment and indicate that E27-binding additionally disturbs STAT2 activation by occupying the IRF9 binding interface. For the first time, these data provide structural insights into cytomegalovirus-encoded interferon antagonism and establish an atomic model for STAT2 counteraction by CRL4 misappropriation with important implications for viral immune evasion.

Keywords: Interferon; ubiquitin-proteasome system; Cullin-RING ubiquitin ligases (CRL); DDB1; DCAFs; viral DCAF (vDCAF); antiviral; cytomegalovirus (CMV); STAT2; IRF9

Introduction

Human cytomegalovirus (HCMV; Human herpesvirus 5) is the prototypic member of the *Betaherpesvirinae* and a ubiquitous human pathogen. More than three quarters of the global population are latently infected with HCMV (Virgin et al., 2009). HCMV infections usually progress subclinically in healthy adults, but cause mortality and morbidity in immunocompromised individuals such as newborns, AIDS patients, transplant recipients, and the elderly (Griffiths and Reeves, 2021). During host adaptation, cytomegaloviruses became strictly species-specific. Therefore, meaningful *in vivo* experiments cannot be performed with HCMV in unmodified small animal models. This roadblock for basic research and preclinical development is circumvented by studying closely related betaherpesviruses such as mouse cytomegalovirus (MCMV; Murid herpesvirus [MuHV] 1) and rat cytomegaloviruses (RCMVs; MuHV-2 and MuHV-8) (Brizic et al., 2018; Geyer et al., 2015; Voigt et al., 2007) in their corresponding host species. Since MuHV infections represent some of the few genuine virus infection models in which the animal host is infected with its natural pathogen (Becker et al., 2007), they became well-established and broadly applied models in virology and immunology, enabling insights regarding general phenomena of virus pathogenesis and host immunity (Reddehase and Lemmermann, 2018).

Upon encounter of pathogens such as cytomegaloviruses, cytokines called interferons (IFN) are expressed (Ivashkiv and Donlin, 2014; Panne et al., 2007; Schneider et al., 2008) which elicit potent antiviral activity (Isaacs and Lindenmann, 1957) by changing the cellular transcriptome and proteome (Megger et al., 2017; Trilling et al., 2013). In addition to the antiviral activity executed within infected host cells, IFN also orchestrate cellular immune responses (Baranek et al., 2012). IFNs bind to cell surface receptors that are associated with *janus kinases* (JAK) (Darnell et al., 1994) which then phosphorylate intracellular receptor chains, generating docking sites for the *signal transducer and activator of transcription* (STAT). After phosphorylation by JAKs (Levy and Darnell, 2002), STATs homo- and heterodimerise and form transcription factor complexes that translocate into the nucleus where they induce the expression of IFN-stimulated genes (ISGs). Type I IFNs (IFN-I) and type III IFNs (IFN-III) signal through STAT1/STAT2 heterodimers which recruit *IFN regulatory factor 9* (IRF9) to generate the active *IFN-stimulated gene factor 3* (ISGF3) that binds IFN-stimulated response elements (ISRE) in the nucleus (Horvath et al., 1996; Kotenko et al., 2003; Qureshi et al., 1995). IFNγ, the only known type II IFN (IFN-II), mainly signals via phosphorylated STAT1 homodimers that recognise gamma-activated DNA sequences (GAS) and express a distinct set of ISGs. Accordingly, STAT2 is crucial for IFN-I and IFN-III signalling. Furthermore, STAT2 directly and indirectly affects IFN-II signalling, e.g., as part of IFNγ-induced ISGF3 complexes (Le-Trilling et al., 2018; Matsumoto et al., 1999; Trilling et al., 2013; Trilling et al., 2011; Zimmermann et al., 2005), as unphosphorylated IRF9-STAT2 heterodimers (Blaszczyk et al., 2015; Platanitis et al., 2019), and by regulating STAT1 expression levels (Hambleton et al., 2013; Ho et al., 2016; Park et al., 2000). Accordingly, animals and

humans lacking STAT2 are severely immunosuppressed and show an exaggerated susceptibility to infections (Gowen et al., 2017; Hambleton et al., 2013; Le-Trilling et al., 2018; Park et al., 2000).

The pivotal role of STAT2 for IFN signalling and innate immunity shaped virus evolution. Several relevant pathogens escape from an IFN-induced antiviral state by targeting STAT2. For example, Zika virus (ZIKV) (Grant et al., 2016), Dengue virus (DENV) (Ashour et al., 2009; Jones et al., 2005), paramyxoviruses (Parisien et al., 2001; Parisien et al., 2002), MCMV (Trilling et al., 2011; Zimmermann et al., 2005), and HCMV (Le-Trilling et al., 2020) induce STAT2 degradation along the ubiquitin proteasome pathway (UPS). Intriguingly, the responsible virus proteins act as adapters that place STAT2 into the sphere of influence of cellular ubiquitin ligases (UbL) (Barik, 2022; Le-Trilling and Trilling, 2020; Ulane and Horvath, 2002).

The MCMV protein pM27 was the first CMV STAT2 antagonist to be described (Zimmermann et al., 2005). MCMV mutants lacking *M27* are severely attenuated *in vivo* (Le-Trilling et al., 2018; Zimmermann et al., 2005) due to the inability to interfere with STAT2-dependent IFN signalling as evident from the restored replication in STAT2-deficient mice (Le-Trilling et al., 2018). Mechanistically, pM27 binds DDB1, a component of host Cullin4-RING UbLs (CRL4), to induce poly-ubiquitination of STAT2, resulting in its rapid proteasomal degradation (Landsberg et al., 2018; Trilling et al., 2011). While the aforementioned complex formation has been confirmed in several models and by different techniques, direct binding of pM27 to DDB1 and/or STAT2 in absence of other proteins has not been documented yet. This is relevant since paramyxoviral IFN antagonists bind one STAT and induce degradation of another, e.g., STAT1 is needed by human parainfluenza virus 2 to target STAT2 while STAT2 is required for both simian virus 5 (SV5) and mumps V proteins to target STAT1 (Ulane et al., 2005). Structural details regarding the interactions between CRL4, STAT2, and CMV antagonists are currently not available.

CRL4, similar to other CRLs, are modular complexes, comprising a core formed by the cullin scaffold (CUL4A or CUL4B) and a catalytic RING domain subunit (ROC1). Via the adapter protein DDB1, the core is connected to various exchangeable substrate receptors called DDB1- and CUL4-associated factors (DCAFs), forming various cellular CRL4 UbLs with different specificities (Zimmerman et al., 2010). CRLs are regulated by cycles of activation through modification of the cullin C-terminus with NEDD8 ("neddylation"), followed by de-neddylation of substrate-free CRLs and substrate receptor exchange (Baek et al., 2020; Cavadini et al., 2016; Goldenberg et al., 2004; Harper and Schulman, 2021; Reichermeier et al., 2020). Among CRLs, CRL4 exhibit unique features like the presence of the co-adaptor DDA1, which stabilises at least certain substrate receptors on CRL4 by bridging them to DDB1, as in the case of DCAF15 (Bussiere et al., 2020; Du et al., 2019; Faust et al., 2020; Olma et al., 2009; Shabek et al., 2018), and the existence of a flexible hinge in the DDB1 adapter that allows for rotation of the catalytic subunit around the substrate receptor, thus creating a broad ubiquitylation zone to accommodate substrates of different size and shape (Banchenko et al., 2021; Fischer et al., 2014; Fischer

et al., 2011). Most likely, the latter property makes CRL4 a frequent target for viral exploitation to steer antiviral host factors efficiently into the ubiquitin-proteasome pathway. In addition to CMV pM27, there are further examples of viral CRL4-binders that induce host protein degradation such as CMV RL1 (Nightingale et al., 2022; Nobre et al., 2019), pUL35 (Salsman et al., 2012), pUL145 (Le-Trilling et al., 2020), hepatitis B virus X (HBx) (Decorsiere et al., 2016), paramyxovirus V (Precious et al., 2005), and the accessory proteins Vpx and Vpr from immunodeficiency viruses (Greenwood et al., 2019; Schwefel et al., 2015; Schwefel et al., 2014). Mechanistic studies of these viral CRL4 subversion processes yield direct molecular insight into virus adaptation to host replication barriers, advancing the understanding of virus pathology and potentially paving the way for therapeutic opportunities (Becker et al., 2019).

Here, we pursued a proteomic approach to assess RCMV-dependent protein regulation and identified STAT2 as one of the most thoroughly down-regulated factors. The RCMV protein E27 was necessary for reduction of STAT2 protein levels by a process sensitive to the inhibition of the proteasome or CRLs. Moreover, biochemical reconstitution demonstrated that E27 was sufficient for recruitment of STAT2 to the DDB1 adapter protein of host CRL4 complexes. Cryogenic electron microscopy (cryo-EM) structural analyses revealed that E27 replaces endogenous CRL4 substrate receptors, resulting in proper positioning of STAT2 for poly-ubiquitylation and subsequent proteasomal destruction to inhibit host IFN signalling.

Results

RCMV-E E27 down-regulates host STAT2

To uncover RCMV-induced proteome changes, rat embryo fibroblasts (REF) were infected with RCMV-England (RCMV-E). The protein content was analysed after 4 h and 28 h by liquid chromatography coupled to mass spectrometry (LC-MS) and compared to mock-infected controls. In each condition, more than 2300 proteins were quantified in six replicates (Fig. S1A). To our knowledge, this represents the first proteome profiling of RCMV-infected cells. Gene ontology (GO) analysis of the data revealed that only very few ISGs were expressed (Fig. 1A). This under-representation of ISGs among RCMV-induced host proteins strongly suggests the expression of potent RCMV-encoded IFN antagonists. In order to obtain mechanistic insights, we further analysed the relative abundance of IFN signalling proteins. The expression levels of JAK1 and TYK2 kinases were similar to mock-infected cells at both time points (Figs. 1A, S1B). Most strikingly, STAT2 protein levels already started to diminish significantly 4 h post-infection and became virtually undetectable after 28 h of infection (Figs. 1A, S1B), indicating a rapid and sustained RCMV-induced loss of STAT2.

Next, we sought to identify the RCMV-E-encoded factor responsible for the reduction of STAT2 levels. Inspection of the RCMV-E genome (Geyer et al., 2015) revealed 56% sequence identity of E27 to pM27, the factor inducing STAT2 degradation in MCMV infection. To test if E27 accounts for STAT2 down-regulation, an RCMV-E mutant lacking *E27* was constructed by CRISPR/Cas9-mediated mutagenesis resulting in an E27-deficient RCMV-E ("ΔE27"). REF were infected with wild type ("WT") and ΔE27

virus and STAT2 expression was assessed by immunoblot analysis 24 h post infection (p.i.). While WT infection confirmed the MS analysis and caused a complete loss of the STAT2 signal, the ΔE27 virus failed to reduce STAT2 protein concentrations (Fig. 1B). Moreover, the WT-mediated loss of STAT2 proved to be sensitive to treatment with MG132, a proteasome inhibitor, and MLN4924 (Fig. 1B), an inhibitor of the NEDD8-activating enzyme, which shuts off cellular neddylation processes that are essential for CRL activity. These findings strongly suggested an involvement of the ubiquitin-proteasome system in E27-induced STAT2 down-regulation and furthermore indicated the involvement of host CRLs.

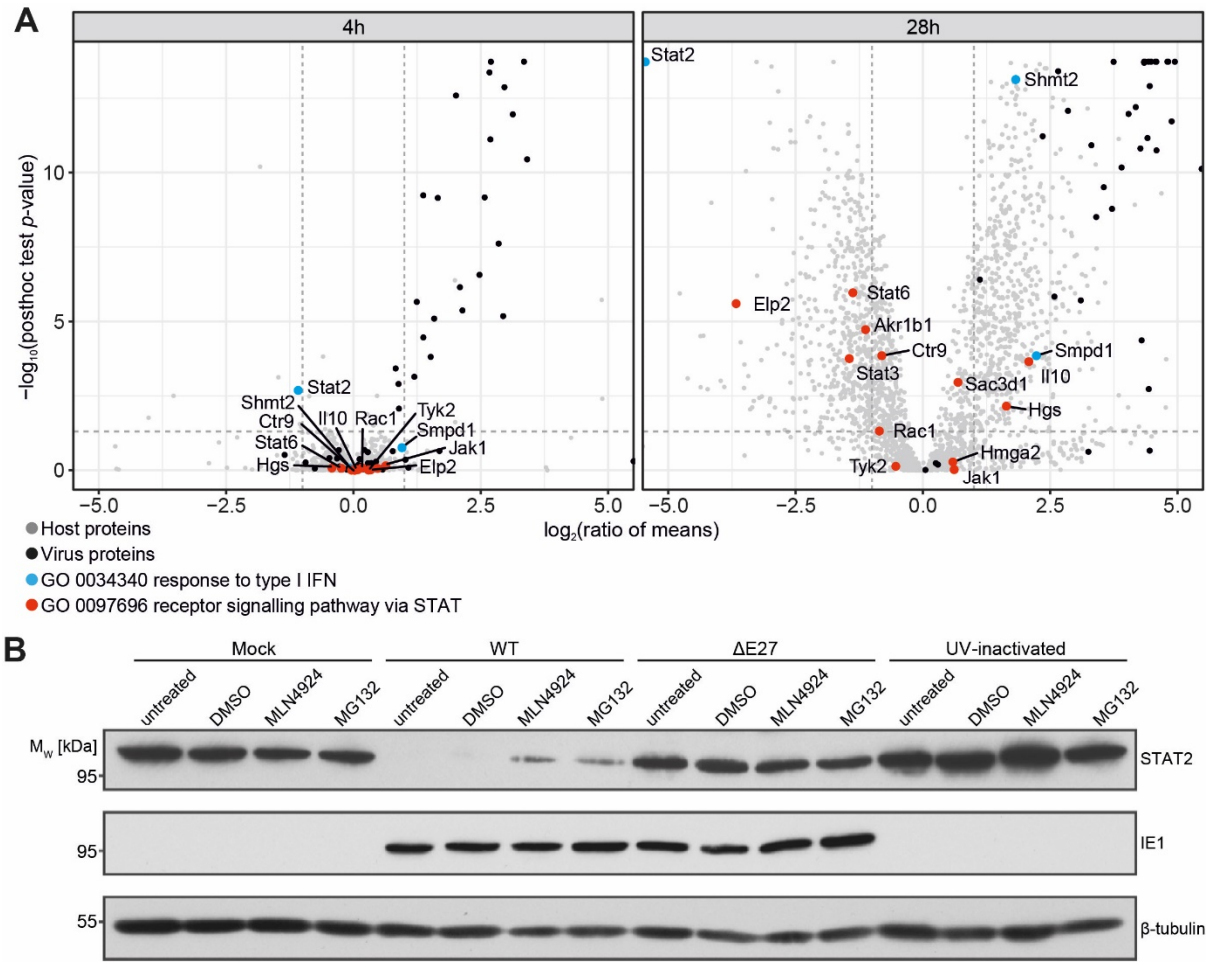

Figure 1: Host protein regulation during RCMV-E infection and the role of E27

(**A**) Mass spectrometric analysis of protein abundance changes upon RCMV-E infection, compared to mock-infected samples. Host and virus proteins are indicated as grey and black dots, respectively. Host proteins involved in the type I IFN response and the STAT signalling pathway are highlighted in blue and red.

(**B**) Western blot analysis of STAT2 protein levels in mock-, WT-RCMV-E-, ΔE27-RCMV-E- or UV-inactivated RCMV-E-infected REF. 24 h p.i., cells were either left untreated or treated for 5.5 h with DMSO, 2.5 µM MLN4924 for blocking the NEDD8-activating enzyme or 10 µM MG132 for proteasome inhibition. IE1 and β-tubulin were used as infection and loading controls.

E27 recruits STAT2 to CRL4 in vitro

These results prompted us to explore the association of E27 with *Rattus norvegicus* (rn) STAT2 and *Homo sapiens* (hs) DDB1 *in vitro*. Importantly, 1128 of 1140 amino acids are identical between hsDDB1 and rnDDB1; the changes are either located in the β-propeller domain B (BPB) of DDB1 (Q494R, I543V, N696T, I704M, D705N) or in disordered loops and regions not involved in intermolecular interactions described below (L29I, L333P, L717I, S738T, T775A, D855G, F1030L). The incubation of DDB1 with equimolar amounts of STAT2, followed by analytical gel filtration (GF) chromatography, resulted in elution in separate peaks at the same elution volumes as the individual proteins in isolation (Fig. 2A, blue, magenta, and grey traces). This argues against intrinsic association of DDB1 and STAT2. In contrast, E27 formed stable binary complexes with STAT2 (Fig. 2B, orange trace) and DDB1 (brown trace). Incubation of E27 together with DDB1 and STAT2 resulted in the elution of all three components in the same peak at an earlier elution volume than the isolated components (Fig. 2A, purple trace). This showed the formation of a stable ternary DDB1/E27/STAT2 protein complex, demonstrating that E27 is sufficient to bridge STAT2 to DDB1.

To obtain complementary information on the topology of the DDB1/E27/STAT2 complex, and to determine a possible involvement of the CRL4 co-adapter DDA1 in E27 and/or STAT2-binding, cross-linking mass spectrometry (CLMS) was performed. DDB1 lacking its β-propeller (BP) domain B ($DDB1_{\Delta BPB}$) was assembled with hsDDA1 (98% identical to rnDDA1), E27 and STAT2 *in vitro* and purified by GF. Subsequently, the complex was cross-linked using the UV-activated cross-linker sulfo-SDA, followed by trypsin digestion and analysis of cross-linked peptides by CLMS. Twenty-eight and 96 heteromeric cross-links were identified between $DDB1_{\Delta BPB}$ and E27, and between E27 and STAT2, respectively, while only 1 cross-link between $DDB1_{\Delta BPB}$ and STAT2 was found (Fig. 2C). These data are in line with a model where E27 serves as connector between DDB1 and STAT2 and indicate that the DDB1 BPB is dispensable for the DDB1/E27/STAT2 complex formation. Furthermore, 69 and 21 cross-links were found between DDA1 and $DDB1_{\Delta BPB}$ or E27, respectively, but no cross-links extended from DDA1 to STAT2 (Fig. 2C). These observations argue for a role of DDA1 in stabilisation of the DDB1/E27-interaction, but against its involvement in the STAT2 recruitment.

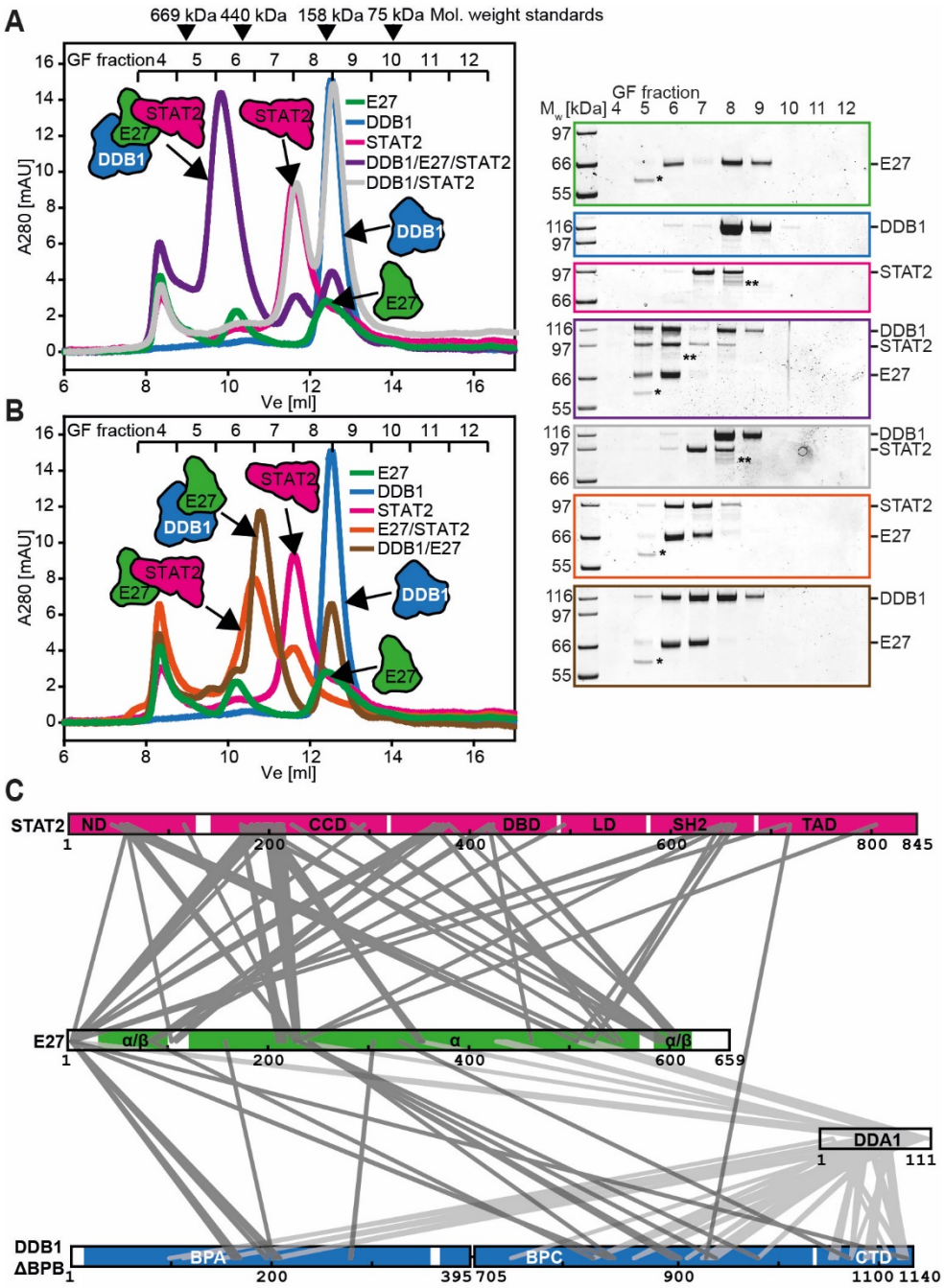

Fig. 2*: In vitro* reconstitution and CLMS analysis of DDB1(/DDA1)/E27/STAT2 protein complexes

(**A, B**) GF analysis of *in vitro* reconstitutions containing the indicated proteins or protein combinations. Coomassie blue-stained SDS-PAGE analyses of fractions collected during the GF runs are shown next to the chromatograms. * - contaminant from E27 preparation; ** - contaminant from STAT2 purification.

(**C**) Schematic of proteins used for CLMS analysis with domains annotated. Heteromeric cross-links obtained from CLMS involving DDA1 are shown as light grey lines, otherwise as dark grey lines. ND – N-terminal domain, CCD – coiled-coil domain, DBD – DNA-binding domain, LD – linker domain, SH2 – Src homology 2, TAD – transactivation domain, BP – β-propeller, CTD – C-terminal domain.

The E27 structure reveals a conserved zinc-binding motif of functional importance

Cryo-EM imaging of a cross-linked $DDB1_{\Delta BPB}$/DDA1/E27/STAT2 complex (Fig. S2) was pursued to gain structural insights. Single particle analysis yielded a density map at 3.8 Å resolution (map 1) (Table S1, Fig. S3) of sufficient quality to generate an E27 molecular model assisted by CLMS distance restraints and *in silico* structure prediction using AlphaFold2 (Jumper et al., 2021) (Figs. 3A, S4A). E27 is composed of two domains, the first being smaller and globular, formed by the N- and C-termini, containing a central four-stranded β-sheet, surrounded by two α-helices (α/β-domain). The larger domain (α-domain) comprises amino acid residues 120-570 folding into an elongated bundle containing 18 α-helices. A prominent structural feature was a protrusion from the edge of the α-domain, mainly formed by helix α8 (Figs. 3A, B, S4B).

The cryo-EM density revealed a cryptic zinc-binding motif in E27, involving three cysteines (C273, C275, C278) and H332 from a loop upstream of helix α9 (Fig. 3C), anchoring the protrusion to the α-domain bundle. The sequence conservation of this motif argues strongly in favour of its functional relevance (Fig. 3D), which prompted us to investigate its function in closely related cytomegaloviruses. MCMV M27, the closest E27 homologue, exhibits 56% and 76% amino acid sequence identity and similarity, respectively (Fig. S4B). E27 and M27 AlphaFold2 structure predictions are almost indistinguishable (RMSD of 1.195 Å, 6652 aligned atoms) (Figs. 3B, S4A), and structural alignment of these predictions demonstrated conservation of side chain positions involved in zinc-binding (Fig. 3C). Thus, M27 represents a valid model to study functional consequences of interference with the zinc coordination motif through site-directed mutagenesis, and to test the predictive power of our E27/M27 model.

First, in FLAG-tagged M27 constructs, individual residues and combinations in the zinc-binding site were mutated to alanine. The constructs were expressed in 293T cells and their ability to bind endogenous DDB1 was assessed by co-immunoprecipitation. While WT-M27 efficiently co-precipitated DDB1, mutation of the three zinc-coordinating cysteine residues abrogated DDB1-binding (Fig. 3E). Likewise, mutation of the loop containing the zinc ligand H333 and of an adjacent LP motif interfered with DDB1-interaction. Serving as an additional control, the Y270F mutation upstream of the cysteine triad had no effect on DDB1-binding. Thus, the integrity of the zinc-binding motif is necessary for interaction with DDB1.

Next, MCMV mutants lacking M27 ("ΔM27") or carrying the AxAxxA triple cysteine mutation ($M27_{AxAxxA}$) were prepared. Immortalised mouse embryonic fibroblasts were infected with these viruses alongside WT-MCMV as a control. STAT2 protein levels of cell lysates were probed by western blot. As expected, WT-MCMV infection resulted in STAT2 depletion. In contrast, the $M27_{AxAxxA}$-MCMV failed to reduce STAT2 protein levels, phenocopying the ΔM27 virus (Fig. 3F). In addition, to test the impact of these MCMV variants on ISG induction, NIH3T3 cells stably expressing an interferon-stimulated response element (ISRE)-dependent luciferase reporter were infected with WT, ΔM27, and

$M27_{AxAxxA}$ viruses. Cells were treated with IFN, and luciferase activity was quantified as proxy for IFN-driven reporter gene expression. Following WT-MCMV infection, IFN signalling was efficiently supressed. ΔM27-MCMV failed to counteract IFN-induced ISRE signalling. The $M27_{AxAxxA}$-MCMV infection exhibited strongly attenuated IFN inhibition (Fig. 3G). These data demonstrate that the disruption of the M27 zinc-binding site interferes with M27-dependent STAT2 degradation, and alleviates but not fully abrogates suppression of IFN responses.

To assess the relevance of these observations *in vivo*, mice were infected with WT-, ΔM27-, or $M27_{AxAxxA}$-MCMVs, and virus titres in salivary glands were determined. Virus titre in ΔM27- and $M27_{AxAxxA}$-MCMV infection were reduced strongly in comparison to WT-MCMV (Fig. 3H). This stresses the importance of M27 for MCMV replication and shows that the $M27_{AxAxxA}$ mutation to a large extent phenocopies the *M27* deletion also in the mouse model. In conclusion, the disruption of the M27 zinc-binding motif causes a loss of DDB1 binding and STAT2 degradation, an impairment of IFN antagonism and ultimately a virus attenuation *in vivo,* connecting our atomic model with the CMV *in vivo* replication capacity.

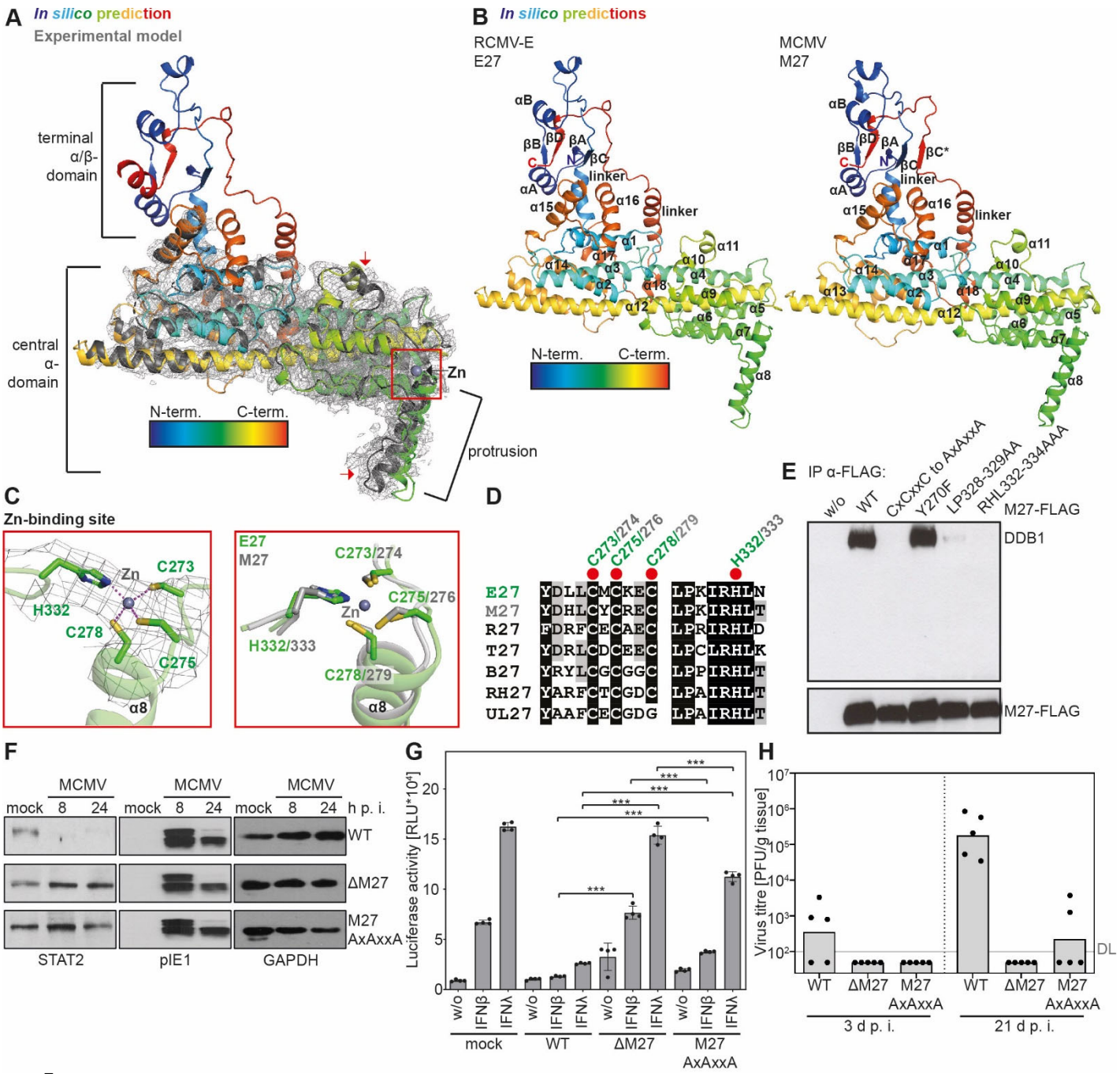

Figure 3: E27 structure reveals a conserved zinc-binding motif

(A) Superposition of the AlphaFold2 E27 model (rainbow-coloured from N- to C-terminus) with a partial structure (grey) manually built into cryo-EM map 1 (Fig. S3). Structures are shown as cartoons. Terminal regions of the AlphaFold2 model with very low confidence have been removed for clarity. Cryo-EM map 1, contoured at 5σ, is shown as grey mesh. Red arrows indicate regions with significant structural differences between predicted and experimental model. The black arrow and the red box indicate the zinc-binding motif. The zinc ion is shown as grey sphere.

(B) Cartoon representation of AlphaFold2 models of E27 (left) and M27 (right), coloured as in **A**. Terminal regions with very low confidence have been removed. Termini and secondary structure elements are labelled.

(C) Detailed view of the zinc-binding motif highlighted in **A**. E27 is shown as green cartoon, residues involved in zinc-binding as sticks. Zinc coordination bonds are indicated as dashed lines. Cryo-EM density, contoured at 6σ, is shown as grey mesh. The right panel shows a superposition of the E27 (green) and M27 (grey) zinc-binding sites.

(D) Amino acid sequence alignment of E27 and homologues from other CMV species. Residues involved in zinc coordination are marked by red dots.

(E) 293T cells were transfected with M27-FLAG or the indicated M27-FLAG variants. 24 h after transfection, cells were lysed and M27-FLAG was precipitated using a FLAG-specific antibody. Precipitates were separated by SDS-PAGE, blotted and probed using the indicated antibodies.

(F) Mouse fibroblasts were infected with MCMV or the indicated MCMV mutants. At the indicated time points, cells were lysed, proteins were separated by SDS-PAGE and blotted. Blots were probed using the indicated antibodies. pIE1 and GAPDH were used as infection and loading controls.

(G) NIH3T3 reporter cells stably expressing ISRE-Luc were infected with the indicated MCMV strains, treated with IFNβ or IFNλ, and luciferase activity was measured. *** – $P \leq 0.001$ (ANOVA).

(H) BALB/c mice were infected i.p. with WT-MCMV and indicated MCMV mutants. At 3 and 21 d p.i., salivary glands were collected and frozen. Virus titres were determined from organ homogenates by plaque titration. Titrations were performed in quadruplicates. Bars depict the geometric mean, dots show titres of individual mice. DL – detection limit.

The DDB1$_{\Delta BPB}$/E27 protein complex

Next, we focused on structural analysis of the DDB1/DDA1/E27 interaction. No experimental cryo-EM density corresponding to the expected position of DDA1 was observed (Fig. S5A). Based upon distance restraints obtained from CLMS (Fig. 2C), the space accessible for interaction with the centre of mass of the DDA1 C-terminal helix was calculated using the DisVis algorithm (van Zundert and Bonvin, 2015). Visualisation of this space indicates that DDA1 preferably locates to a large, ill-defined DDB1 surface region around the edges of BPC and CTD. These data indicate that DDA1 is flexible and does not stably interact with E27, accounting for the lack of cryo-EM density (Fig. S5B).

However, clear cryo-EM density corresponding to DDB1 BPA and BPC was present, allowing to unambiguously position a molecular model and to analyse the interaction with E27 in detail. E27 binds to a cleft lined by the inner surfaces of DDB1 BPA and BPC (Fig. 4A). In this way, it is positioned on the opposite side of where DDB1 BPB would be located, which links to the CRL4 core. E27 helices α6, α7, α8, and the loop leading to α9 are in direct contact with DDB and helix α8 protrudes in the binding cleft (Fig. 4A, B). Eleven out of the 28 heteromeric cross-links from CLMS could be mapped on the DDB1/E27 structure. In support of the model, most cross-links are within the 25 Å distance threshold enforced by the cross-linker chemistry, with only two slight outliers (26 Å and 32 Å) (Fig. 4B, Fig. S6, Table S2).

The DDB1/E27 binding interface, covering an area of 2064 $Å^2$, is divided in three regions (Fig. 4A, C). The first involves E27 helices α6 and α7, bordered by the zinc-coordinating cysteine triad, contacting residues located in DDB1 BPC WD40 repeats 6 and 7, and in the CTD. It is formed by a network of hydrogen bonds, additionally supported by salt bridges and hydrophobic interactions (Fig. 4C, box I). A second, central interaction region includes the protrusion formed by helix α8 and a subsequent polybasic loop, contacting residues lining the inner surface of DDB1 BPC and BPA WD40 repeats 3 and 7. This interface is mostly hydrophobic, with fewer polar and electrostatic interactions (Fig. 4C, box II). A third region comprises the extended loop leading back to the E27 zinc-binding motif, adjacent to DDB1 BPA WD40 repeats 3 and 4. Again, mainly hydrophobic interactions form this interface, assisted by hydrogen bonding (Fig. 4C, box III).

To evaluate the conservation of the DDB1/E27-binding surface, we mapped interface residues on a multiple sequence alignment of E27 homologues (Fig. 4D). Twenty-four out of 33 interfacing residues are type-conserved between RCMV-E E27 and MCMV M27, while 22 are type-conserved between E27 and R27, the homologue encoded by RCMV-Maastricht (RCMV-M). Furthermore, 11 and 10 interface residues are type-conserved in E27 homologs from bat and tupaiid CMV, respectively, and only three residues in rhesus macaque CMV and HCMV. Additionally, in the case of tupaiid, bat, rhesus macaque, and human CMV, high sequence divergence of the central α8 binding region is apparent. Together, this suggests that DDB1-binding functionality is restricted to rodent CMV E27, M27 and R27.

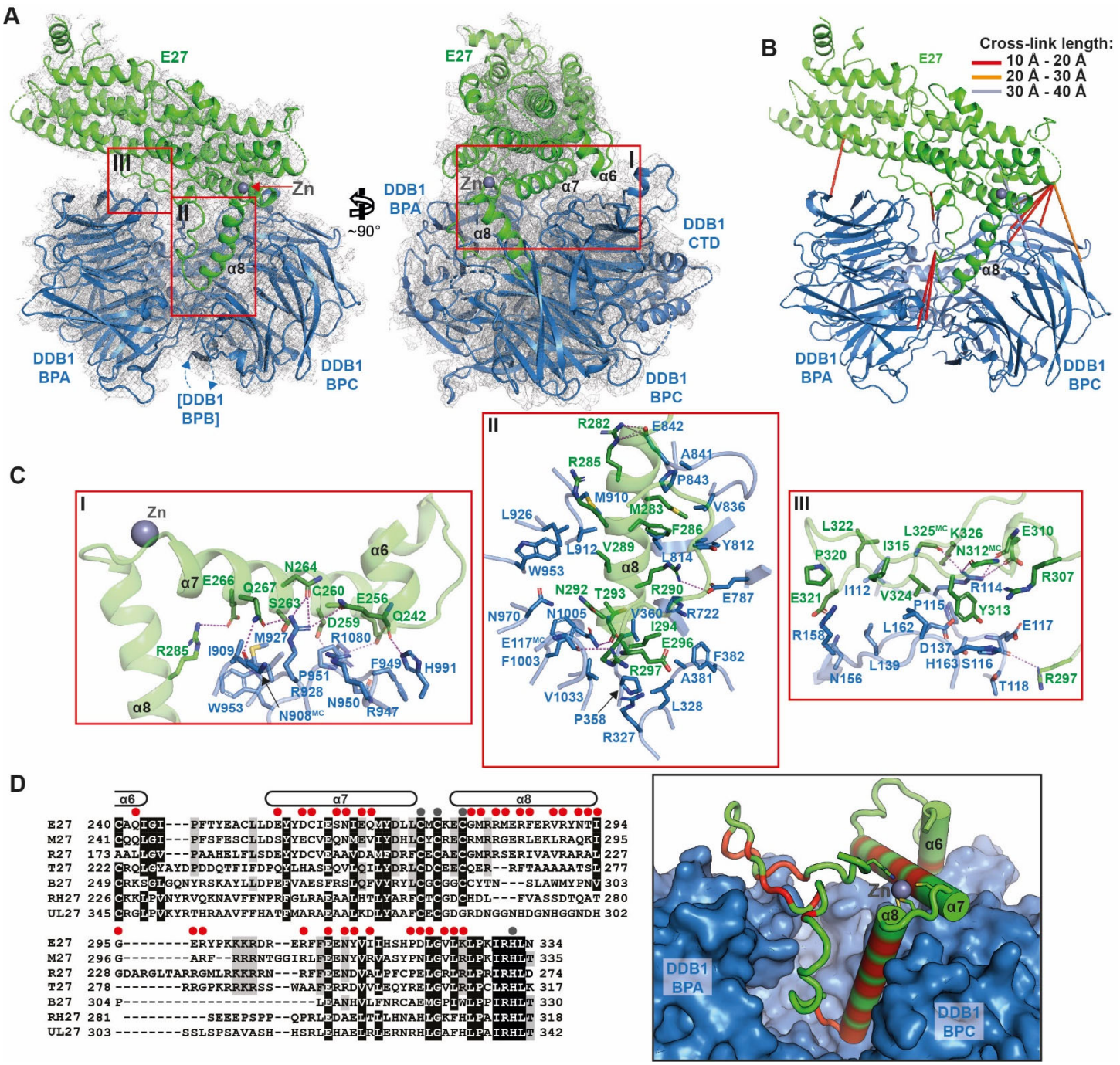

Figure 4: The DDB1$_{\Delta BPB}$/E27 protein complex

(A) Structure of the DDB1$_{\Delta BPB}$/E27 complex in two views. Proteins are shown as cartoons; DDB1$_{\Delta BPB}$ is coloured blue and E27 green, the zinc ion shown as grey sphere. Regions involved in DDB1$_{\Delta BPB}$/E27 interaction are boxed. Cryo-EM density map 1 (Fig. S3), contoured at 5σ, is shown as grey mesh.

(B) Intermolecular sulfo-SDA cross-links were mapped on the DDB1$_{\Delta BPB}$/E27 structure shown in **A**, colour-coded according to their length as indicated.

(C) Detailed view of regions of interest indicated in **A**. Selected amino acid residues involved in intermolecular contacts are shown as sticks. Dashed lines represent hydrogen bonds or salt bridges. MC – main chain.

(D) Left panel: amino acid sequence alignment of E27 and homologues from other cytomegaloviruses. E27 residues contacting DDB1 are indicated by red dots and residues involved in zinc coordination as grey dots. E27 secondary structure elements are drawn above the alignment. Right panel: simplified visualisation of DDB1-interacting E27 residues and secondary structure elements shown in the alignment.

E27 mimics endogenous CRL4 substrate receptors

Next, the DDB1/E27 complex structure was compared to the DDB1-binding modes of DCAF1 and of the previously characterised viral DCAFs (vDCAFs) SV5 V and HBx. Overall, they are positioned similarly relative to DDB1 (Fig. 5A). Analysis of their "molecular footprint" on DDB1 reveals that the E27 footprint is almost identical to the DCAF1-derived one, while SV5 V and HBx bind DDB1 in significantly smaller interaction interfaces, mostly restricted to DDB1 BPC (Fig. 5B). E27 utilises different structural elements to engage DDB1 surface regions than DCAF1, i.e. a short and two long helices (α6-α8) and an extended loop, in contrast to three short helices and the bottom side of four WD40 repeats in DCAF1 (Fig. 5A, insets). Superposition of DDB1-bound E27 and (v)DCAF structures showed that the only common secondary structure element is the C-terminal half of E27 α8, which aligns well with a short helical "H-box" motif in DCAF-type receptors (Fig. 5C). However, sequence conservation of this motif is low, with only 3 amino acid positions >60% type-conserved (Fig. 5D). Together, these data demonstrate how E27 emulates the DDB1-binding mode of endogenous DCAF substrate receptors using divergent structural principles. Furthermore, the analysis illustrates that all examined vDCAFs engage DDB1 via additional structural elements beyond the previously described "H-box" motif (Li et al., 2010). However, their structure and sequence are not conserved, and the only common characteristics are contact areas on the upper edge of DDB1 BPC.

Given the similar position and interface area of E27 and DCAF1 on DDB1, we hypothesised that E27 competes with endogenous DDB1/DCAF complexes for DDB1-binding. To gain biochemical insight, the pre-formed DDB1/DCAF1 complex was incubated with E27 and subjected to analytical GF. These analyses showed the formation of an elution peak containing DDB1 and E27, concomitant with reduction of the DDB1/DCAF1 complex peak at later elution volume, in an E27 concentration-dependent manner, indicating that E27 is able to displace DCAF1 from DDB1 *in vitro* (Fig. 5E).

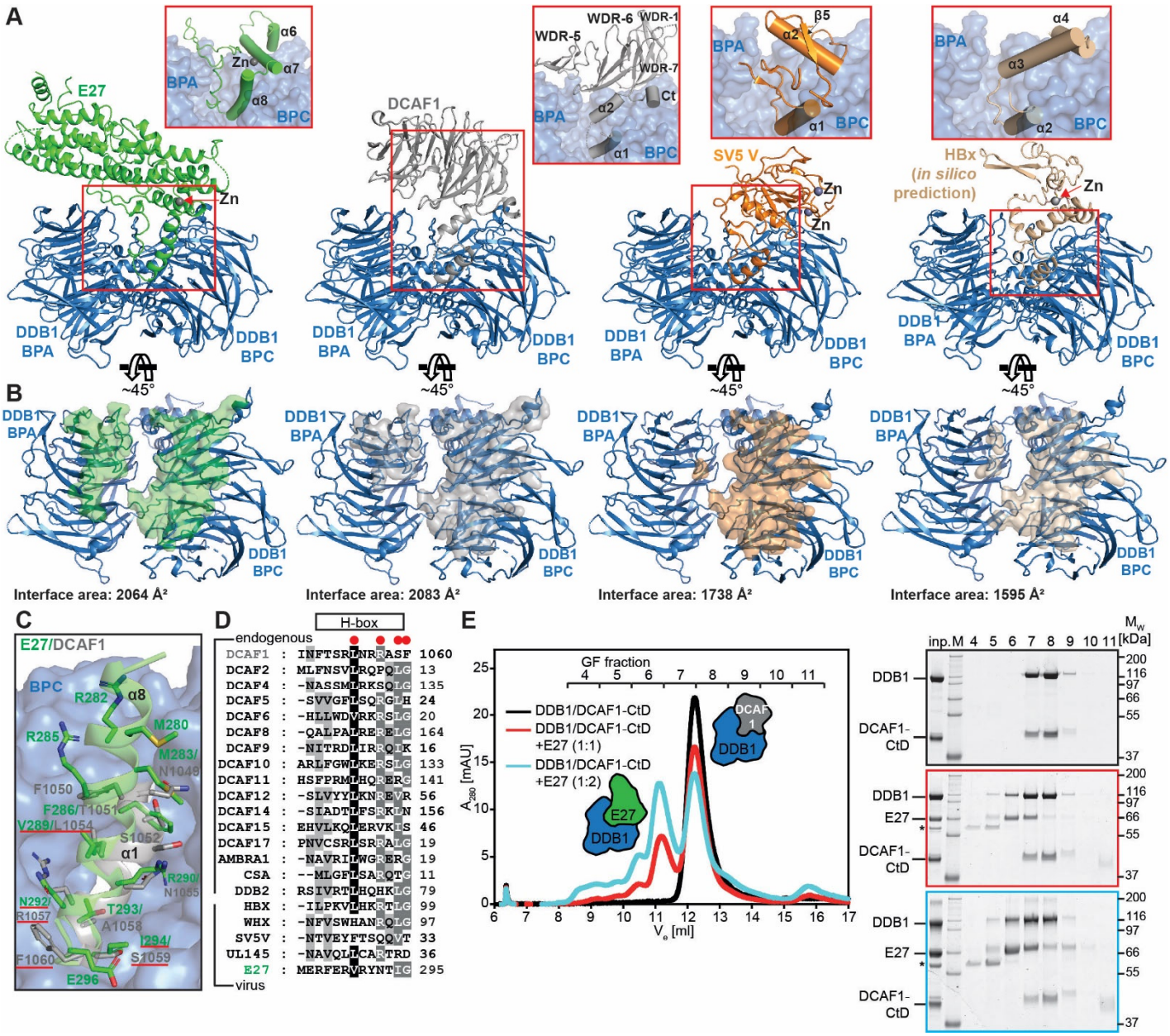

Figure 5: E27 replaces endogenous CRL4 substrate receptors

(A) Comparison of the DDB1/E27-binding mode with endogenous and viral CRL4 substrate receptors. Structures of DDB1 (blue) in complex with E27 (green), DCAF1 (grey, PDB 6zue (Banchenko et al., 2021)), SV5 V (orange, PDB 2hye (Angers et al., 2006)) and HBx (wheat, AlphaFold2 prediction, Fig. S4C) are shown as cartoons. Regions of the AlphaFold2 HBx model with very low confidence have been removed. The insets display enlarged views of the boxed interaction areas, with DDB1 shown as semi-transparent blue surface. Zinc ion are shown as grey spheres. The position of the HBx zinc ion was modelled based upon information from (Ramakrishnan et al., 2019).

(B) "Molecular footprint" of substrate receptors from **A** on the DDB1 surface. DDB1 is shown in the same representation as in **A**, but slightly rotated to allow unobstructed view of the receptor-binding cleft. The receptors themselves have been removed for clarity. Parts of the DDB1 surface in contact with the respective substrate receptor are coloured according to the scheme in **A**.

(C) Detailed comparison of a helical DDB1-binding motif in E27 (green) and the DCAF1 "H-box" (grey). DDB1 is shown as semi-transparent blue surface, E27 and DCAF1 as semi-transparent cartoon. Selected amino acid residues involved in intermolecular contacts are shown as sticks.

(D) Amino acid sequence alignment of the "H-box" DDB1-binding motif in endogenous substrate receptors and viral factors hijacking DDB1. Black boxes: >80% type-conserved; dark grey: >60%; light grey: >40%. >60% type-conserved residues are marked by red dots, and underlined in **C**.

(E) Pre-formed DDB1/DCAF1 protein complex was incubated with indicated amounts of E27 and analysed by GF. SDS-PAGE analyses of GF fractions are shown next to the chromatogram. * - contaminant from E27 preparation.

Mechanism of STAT2-recruitment

Cryo-EM map 1 showed extra density features consistent with the presence of a 4-helix bundle on top of E27, opposite of the DDB1-binding interface (Fig. S3). Moreover, further 3D classification of the cryo-EM particle images yielded a second map at 5 Å resolution, exhibiting more density in that region (map 2, Fig. S3, Table S1). This allowed the placement of a STAT2 AlphaFold2 model lacking the N-terminal and TAD domains, and enabled fitting of the E27 α/β-domain, revealing that E27 recruits STAT2 using a bipartite binding interface (Fig. 6A). It comprises a central interaction between the STAT2 coiled-coil domain (CCD) and the E27 α-domain, as well as a second contact region involving the STAT2 DNA-binding domain (DBD) and the E27 α/β-domain (Figs. 6A, B, S4B). Thirty-five out of 96 heteromeric cross-links could be mapped on the E27/STAT2 complex, of which 23 lie within the 25 Å distance threshold, supporting the structural data. Few severely overlength cross-links are apparent (>50 Å), which involve the E27 α/β-domain or the STAT2 SH2 domain, indicating flexibility of these distal components (Fig. 6B, Fig. S6, Table S2), explaining the low local resolution of the corresponding cryo-EM map regions (Fig. S3).

The central STAT2 CCD/E27 α-domain interaction covers a surface area of 817 $Å^2$. It comprises hydrophobic residues from STAT2 CCD helices αA, αB, and the loop C-terminal of αC. These residues project into a hydrophobic pocket lined by E27 amino acids from the loop downstream of α4 and side chains from a sequence stretch spanning α11 to α12. In addition, several peripheral hydrogen bonds and a salt bridge network strengthen the interface (Fig. 6C). The second E27/STAT2 interaction area involves parts of the E27 α/β-domain, located between strand βA and helix αA, between αB and βC, and a C-terminal stretch upstream of βD (Fig. S4B). These regions form a shallow surface which contacts a contiguous STAT2 DBD protrusion comprising amino acid residues 365-373, 377-383, and 406-418. Due to the low local resolution of the cryo-EM map, we refrained from modelling individual side chain interactions.

Conservation analysis of the central STAT2-binding interface revealed that out of 17 involved residues, 10 are type-conserved in rodent E27 homologues (M27, R27), while only 5-6 are type-conserved in their

tupaiid, bat, macaque or human counterparts (Fig. 6D). Additionally, in these more distantly related CMV species, most of the VPVL loop downstream of α4 is deleted, removing a significant portion of the STAT2-binding site. Thus, it is likely that STAT2 recruitment is restricted to rodent E27 homologues. Variation within this branch might be driven by species-specific adaptation to differences in the respective host STAT2 sequences, e.g. rnSTAT2 positions 169 and 286 (Fig. 6D).

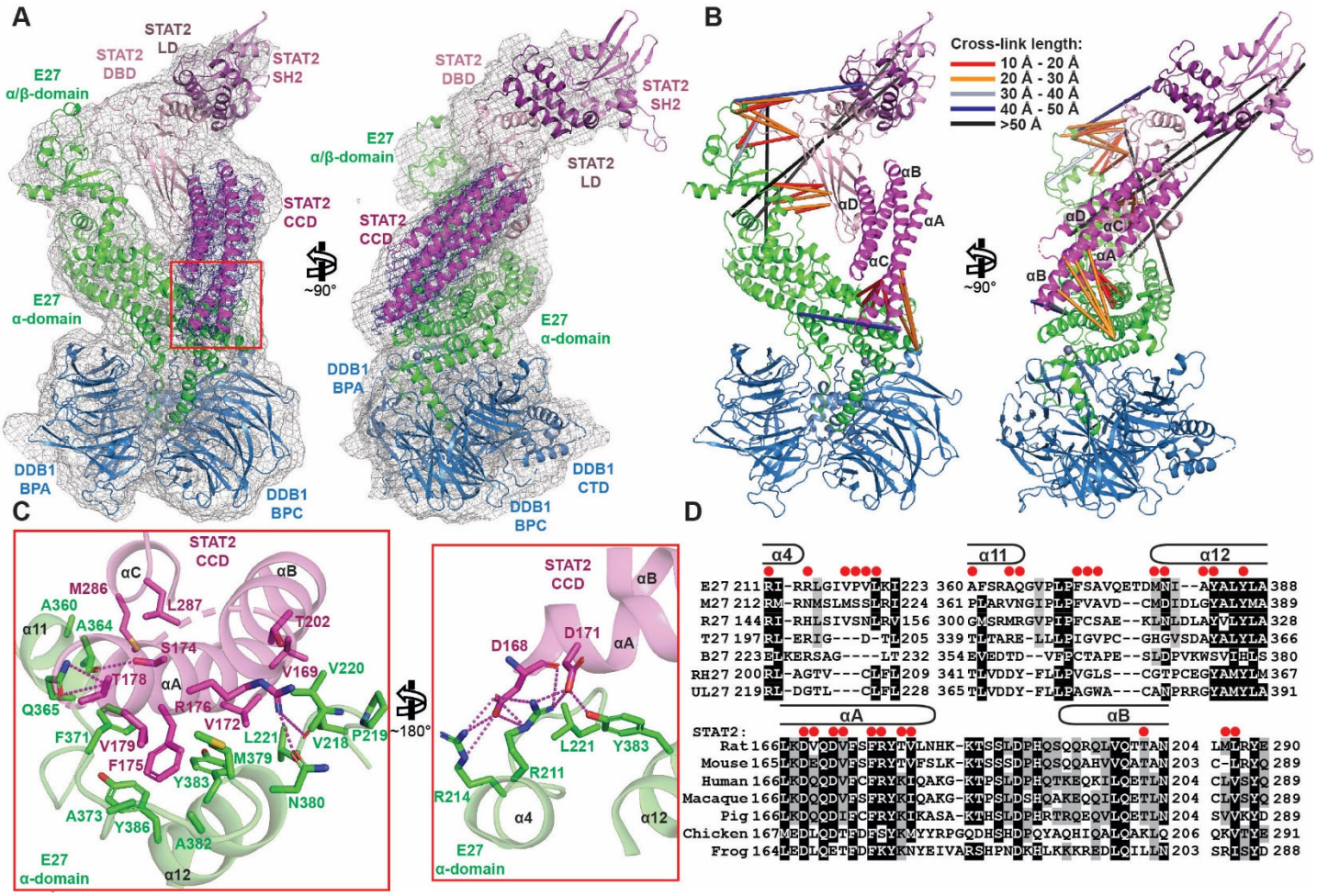

Figure 6: Mechanism of STAT2 recruitment

(A) Structure of the $DDB1_{\Delta BPB}$/E27/STAT2 complex. Proteins are represented as cartoons; $DDB1_{\Delta BPB}$ is coloured blue, E27 green, STAT2 magenta and the zinc ion shown as grey sphere. Experimental cryo-EM map 2 (Fig. S3), contoured at 4σ, is shown as grey mesh. The portion of map 1 encompassing the STAT2 CCD is shown as blue mesh, contoured at 5σ. The central E27/STAT2 CCD interaction region is boxed.

(B) Intermolecular sulfo-SDA cross-links were mapped on the protein complex shown in **A** and colour-coded according to their length. Protein representation and colour scheme are the same as in **A**.

(C) Detailed view of the region boxed in **A**. E27 and STAT2 are shown in semi-transparent cartoon representation and coloured as in **A**. Selected amino acid residues involved in intermolecular contacts are shown as sticks. The dashed lines represent hydrogen bonds and salt bridges.

(D) Multiple amino acid sequence alignment of the portions of E27 and STAT2 involved in their interaction. Side chains in direct contact with the respective binding partner are indicated by red dots above the alignment.

E27 positions STAT2 appropriately for CRL4-catalysed ubiquitin transfer

The structure of the DDB1/E27/STAT2 complex enabled modelling of STAT2 in the context of a complete CRL4 assembly (Fig. 7A). The model shows that STAT2 is placed centrally in the ubiquitylation zone created by rotation of the CUL4/ROC1 scaffold arm. It also provides a rationale for the existence of the second, auxiliary E27/STAT2 DBD-binding interface, which nudges the STAT2 molecule into the ubiquitylation zone. In such a way, surface-exposed lysines on all STAT2 domains are within reach of ubiquitin-charged E2, which is positioned for ubiquitin transfer by a catalytic assembly comprising the neddylated distal end of CUL4 and ROC1 (Baek et al., 2020), guaranteeing efficient STAT2 ubiquitylation and subsequent degradation.

The E27/STAT2-interaction is incompatible with formation of an active ISGF3 signalling complex

Comparison of the E27/STAT2 CCD binding mode discovered here to the IRF9/STAT2 CCD complex (Rengachari et al., 2018) demonstrates overlap of the binding interfaces (Fig. 7B). Consequently, the STAT2/E27 interaction is sterically incompatible with IRF9-binding, prohibiting formation of an active ISGF3 signalling complex, and providing a second layer of STAT2 inhibition, beyond induction of its proteasomal degradation. Consistent with this, we observed significant residual ISG-suppression in cells infected with a DDB1-binding-deficient MCMV mutant ($M27_{AxAxxA}$) (Fig. 3G).

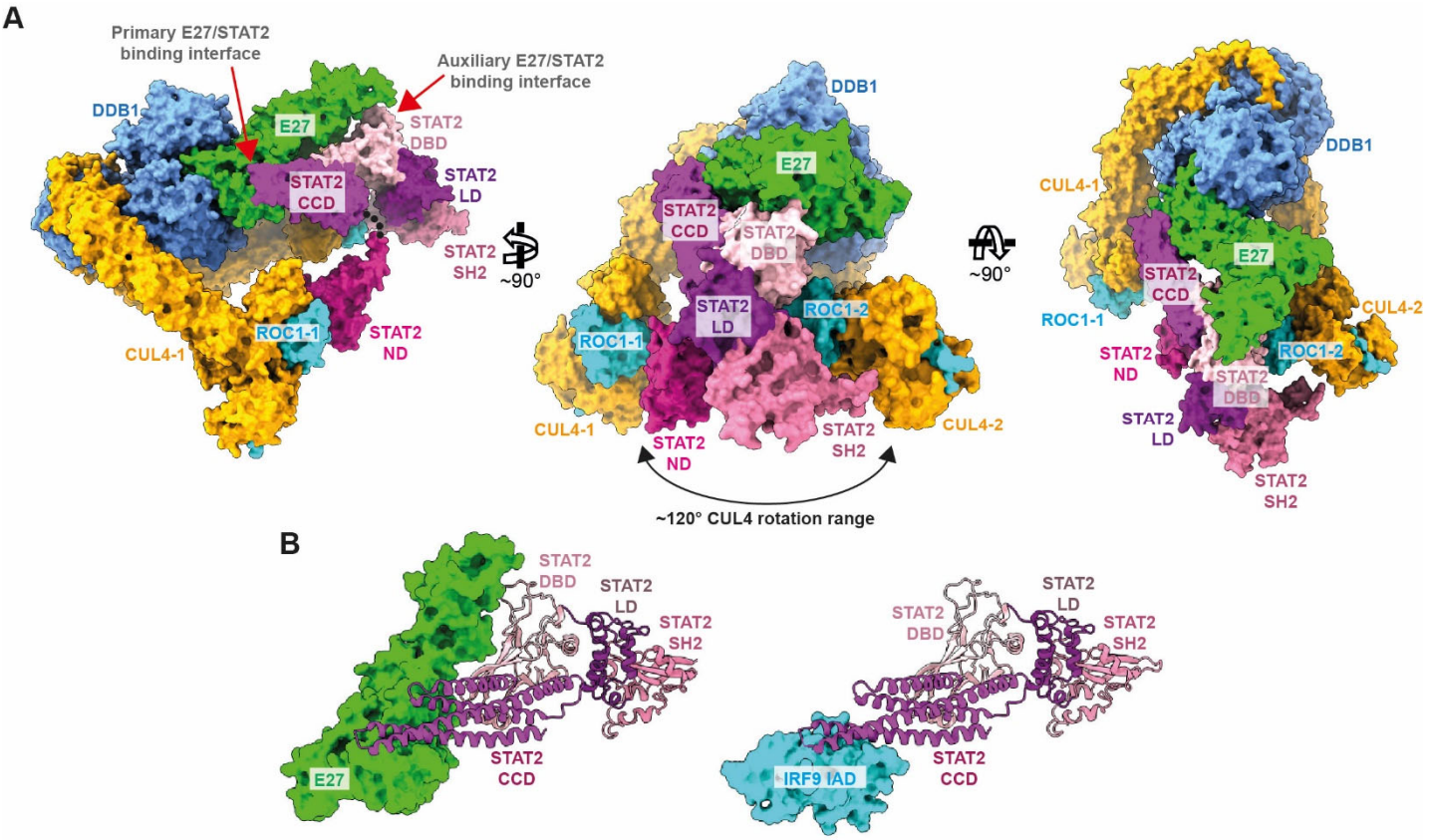

Figure 7: Model of the complete CRL4^{E27}/STAT2 assembly, comparison to STAT2/IRF9 complex

(A) A model of how E27/STAT2 is positioned relative to the remainder of CRL4 was assembled by superposition of $DDB1_{\Delta BPB}$/E27/STAT2 with DDB1 BPA/BPC from two $CRL4^{DCAF1}$ cryo-EM structures, which represent the two outermost positions of the CUL4 scaffold (CUL4-1, CUL4-2), thus visualising the rotation range of CUL4/ROC1 with respect to DDB1 (Banchenko et al., 2021). ROC1 (cyan), CUL4 (orange), DDB1 (blue), E27 (green) and STAT2 (coloured as in Fig. 5) are shown in surface representation. The STAT2 N-terminal domain (magenta cartoon) was modelled in an arbitrary position, since it is connected to the STAT2 CCD via a flexible linker (indicated by the dotted line).

(B) Comparison of STAT2-binding to E27 and IRF9 (PDB 5oen) (Rengachari et al., 2018). STAT2 is shown as cartoon and coloured as in Fig. 5. E27 (green) and the IRF9 IRF-associated domain (IAD, cyan) are shown in surface representation.

Discussion

Here, we identify STAT2, the central hub driving the antiviral IFN response, as the most drastically down-regulated host factor during RCMV-E infection and determine E27 as a responsible factor. The structure determination of E27 uncovered a zinc-binding motif close to the DDB1-binding site that is highly conserved in homologous proteins from related cytomegaloviruses. Disruption of this motif in the closely related E27 homologue pM27 resulted in impairment of DDB1 binding, STAT2 degradation and ISG suppression, and finally to inhibition of virus replication *in vivo*. Similarly, the integrity of conserved zinc-coordinating motifs has been shown to be crucial for CRL4 association and function of SV5 V (Lin et al., 1998) and the retroviral accessory proteins Vpx and Vpr (Wang et al., 2017; Yamamoto et al., 2017). However, HBx side chains involved in zinc coordination are dispensable for CRL4 interaction, but critical for substrate recruitment (Ramakrishnan et al., 2019).

With pUL27, HCMV encodes a positional and sequence homologue of pM27 and E27. HCMV reduces STAT2 levels (Le et al., 2008; Nightingale et al., 2018) and - like MCMV - exploits the UPS and CRLs to this end (Le-Trilling et al., 2016; Le et al., 2008). However, pUL27 is neither essential nor sufficient for the HCMV-induced STAT2 degradation (Le et al., 2008), and at best interacts very weakly with DDB1 (Landsberg et al., 2018; Reitsma et al., 2011; Trilling et al., 2011). Our structure-based sequence alignment shows considerable sequence divergence between rodent E27 homologues and pUL27 in the critical DDB1-binding helix α8, thereby rationalising these observations.

Indeed, the HCMV-encoded STAT2 antagonist was recently identified as pUL145 (Le-Trilling et al., 2020). Like pM27, pUL145 interacts with DDB1 and CRL4 (Nightingale et al., 2018) and induces proteasomal degradation of STAT2 (Le-Trilling et al., 2020). Accordingly, an unbiased single cell sequencing approach combined with a genome-wide CRISPR screen confirmed the central importance of the IFNAR2/STAT2/IRF9 signalling axis as well as neddylation and Cullin-RING UbLs in defining HCMV infection propensity (Hein and Weissman, 2021). Hence, future structural studies of how UL145 integrates into CRL4, and how it recruits STAT2, would be highly informative to fully understand the

different mechanistic principles pursued by HCMV and rodent CMV for STAT2 antagonism, both converging on CRL4.

Comparison of the DDB1-binding modes of E27 and other CRL4 substrate receptors revealed that E27 engages similar surface regions in the DDB1 binding cleft as DCAF-like receptors. However, structure and sequence determinants in E27 and other viral and cellular DCAFs mediating DDB1-binding are highly divergent. This pronounced plasticity impedes sequence-based prediction, and strongly suggests the existence of further, yet unidentified viral and endogenous DDB1-binders. In line with these observations, recent HCMV interactome studies discovered several more DDB1- and CRL4-associated HCMV factors (Nightingale et al., 2022; Nobre et al., 2019). Future studies of DDB1-binding mechanisms, together with proteomics and novel *in silico* structure prediction methods (Humphreys et al., 2021; Jumper et al., 2021), might greatly expand the spectrum of known DDB1-binders and extend our understanding of CRL4 biology and its viral exploitation.

Acknowledgments

This research was supported by the German Research Foundation (DFG) Emmy Noether Programme SCHW1851/1-1 (D.S.), by an EMBO Advanced grant aALTF-1650 (D.S.), and by an iNEXT grant 5419 (D.S.). M.T. receives funding from the DFG through RTG1949, TR1208/1-1 and TR1208/2-1. We thank the MPI-MG for granting access to the TEM instruments of the microscopy and cryo-EM service group; Dominik A. Megger for initial mass spectrometry analyses; Birgit Zülch and Kristin Fuchs for technical support.

Author Contributions

V.T.K.L.-T., S.B., A.G., J.B., T.B., B.S., T.M., J.R., C.M.T.S., S.V., M.T., D.S. planned experiments. V.T.K.L.-T., D.P., S.B., L.B., A.G., C.G., J.B., T.B., B.S., S.V., M.T., D.S. performed experiments. V.T.K.L.-T., D.P., S.B., S.L., A.G., T.B., B.S., J.R., S.V., M.T., D.S. analysed data. S.V., M.T., D.S. wrote the initial draft, all authors reviewed and edited the manuscript.

Declaration of Interests

The authors declare no competing interests.

Methods

Animals

BALB/c mice were obtained from Harlan and bred and housed in the animal facility of the Institute for Virology of the University Hospital Essen. Mice were maintained under selective pathogen-free conditions. Age (8-16 weeks) and sex-matched (male and female) groups of BALB/c mice were infected intraperitoneally with 2x 10^5 PFU of WT-MCMV or MCMV mutants per mouse. All procedures were performed in accordance with the guidelines of the University Hospital Essen, Germany, the national animal protection law (Tierschutzgesetz [TierSchG]) and the recommendations of the Federation of European Laboratory Animal Science Association (FELASA). The study was approved by the Northrhine-Westphalia State Office for Nature, Environment and Consumer Protection (LANUV NRW, Düsseldorf, Northrhine-Westphalia, Germany; permit #84-02.04.2016.A441).

Microbe strains

E. coli NovaBlue and Rosetta™ 2(DE3) were cultivated in LB medium at 37°C in a shaker incubator (150 rpm) (Table S3).

Cell lines

Immortalised mouse fibroblasts were generated from primary C57BL/6 and BALB/c MEF by crisis immortalisation (Rattay et al., 2015). NIH3T3-ISREluc:IFNLR cells were described in (Le-Trilling et al., 2018). Mouse fibroblasts, REF and HEK293T (ATCC CRL-11268, female) cells were grown in Dulbecco`s minimal essential medium (DMEM) supplemented with 10% fetal calf serum (FCS), penicillin, streptomycin, and 2 mM glutamine at 37°C in 5% CO2. Sf9 cells (originally derived from the ovaries of *Spodoptera frugiperda*) were cultivated in Insect-XPRESS™ medium at 28°C in a shaker incubator (180 rpm) (Table S3).

Primary cultures

Organs of infected mice were harvested, snap frozen in liquid nitrogen, and stored at -80°C until titrations were performed. Plaque titrations were conducted by use of primary mouse fibroblasts (mouse embryonic fibroblasts [MEF] and mouse newborn cells [MNC]) which were isolated from mouse embryos and newborns, respectively, according to described protocols (Le-Trilling and Trilling, 2017). Fibroblasts were grown in DMEM supplemented with 10% (v/v) FCS, 100 µg/ml streptomycin, 100 U/ml penicillin, and 2 mM glutamine. All cell culture media and supplements were obtained from Gibco/Life technologies.

Viruses

WT-RCMV-E has previously been described (Ettinger et al., 2012). ΔE27-RCMV-E was generated by CRISPR/Cas9-mediated genome editing. REF were transduced with a mixture of four CRISPR/Cas9 lentiviral vectors carrying sgRNAs that target viral genome up- and downstream of the E27 gene (see

Table S3). Successfully transduced cells were selected with 2.5 µg/mL puromycin prior to infection with WT-RCMV-E. This resulted in an E27-knockout virus (ΔE27) with a complete deletion of the 1970 bp *E27* gene. E27 deletion was verified by PCR and sequencing. Mutant virus was screened by limiting dilution and was double plaque-purified. WT-MCMV was reconstituted from the BAC described in (Jordan et al., 2011). ΔM27-MCMV has been previously described (Le-Trilling et al., 2018). The $M27_{AxAxxA}$ mutant was generated according to previously published procedures (Tischer et al., 2006; Wagner et al., 2002) using the primers MCMV-M27-QC1-3_1 and MCMV-M27-QC1-3_2 (Table S4). Viral titers were determined by standard plaque titration on primary MEF, REF or MNC.

Plasmids

For CRISPR/Cas9 viral genome editing, crRNA sequences targeting the viral genome up- and downstream of the E27 gene were designed manually or using the CRISPOR website (http://crispor.tefor.net); Designed crRNA sequences are presented in Table S3 and were cloned as sgRNA downstream a human U6 promoter in the pSicoR-CRISPR-PuroR vector (van Diemen et al., 2016). The pHisSUMO-E27 and pHisSUMO-*Rattus norvegicus* (rn)STAT2 expression plasmids were prepared using standard restriction enzyme cloning. Full-length open reading frames were PCR-amplified from cDNA templates using oligonucleotide primers XmaI-E27-fw and SacI-E27-rev or XmaI-STAT2-fw and NotI-STAT2-rev, and ligated in the pHisSUMO plasmid, to generate N-terminal 6xHis-SUMO-fusion proteins. The rnSTAT2 cDNA template was ordered as *E. coli* codon-optimised Strings DNA fragment from ThermoFisher. To generate pAcGHLT-B-3C-*Homo sapiens* (hs)DDB1, the thrombin protease site between the GST purification tag and DDB1 in pAcGHLT-B-hsDDB1 was changed to a 3C protease site using insertion/deletion PCR according to (Hansson et al., 2008), using the oligonucleotide primers 3C-DDB1-A and 3C-DDB1-B. To generate pAcGHLT-B-3C-hsDDB1 ΔBPB (amino acid residues 396-705 replaced with a GNGNSG sequence, the same method was used, with the oligonucleotide primers ΔBPB-A and ΔBPB-B and pAcGHLT-B-3C-hsDDB1 as template. The M27-FLAG expression plasmid was described previously (Trilling et al., 2011). Site-directed mutations were introduced using the M27-QC primers and the QuikChangeII kit (Agilent) according to manufacturer's instructions. For primer sequences, see Table S4. All constructs were verified by Sanger sequencing.

LC-MS/MS Analyses

Liquid chromatography couple to mass spectrometry analyses were performed as described previously (Megger et al., 2017). Briefly, cells were harvested and dissolved in 50 mM ammoniumbicarbonat containing 0.1% (w/v) Rapigest SF Surfactant (Waters, Boston, MA, USA). Four µg proteins per sample were reduced with dithiothreitol for 30 min at 60°C and thereafter alkylated with 15 mM iodoacetamide for 30 min at room temperature. Subsequently, the samples were digested using trypsin (SERVA Electrophoresis, Heidelberg, Germany) in a ratio of 1:20 (w/w) for 16 h at 37 °C. The reaction was stopped by adding trifluoroacetic acid (TFA) to final 1% (v/v) and the precipitated surfactant was

removed by centrifugation at 16.000 x *g* for 10 min. The supernatants were dried by vacuum centrifugation and dissolved in 0.1 % TFA. An amount of 300 ng tryptic peptides per sample was used for LC-MS/MS analysis and injected into an Ultimate 3000 RSLC nanoLC online coupled to an Orbitrap Elite mass spectrometer (both Thermo Scientific). The peptides were concentrated for 7 min on the trap column (Acclaim PepMap 100, 75 µm × 2 cm, C18, 5 µm particle size, 100 Å pore size) using a flow rate of 30 µL/min. Subsequently, the samples were separated on the analytical column (Acclaim® PepMap RSLC, 75 µm × 50 cm, nano Viper, C18, 5 µm particle size, 100 Å pore size) by applying a gradient from 5 to 40% solvent B over 98 min (solvent A: 0.1% (v/v) formic acid; solvent B: 0.1% (v/v) formic acid, 84% acetonitrile) at a flow rate of 400 nL/min. The column oven temperature was 60°C. Full scan MS spectra were acquired in the Orbitrap analyzer at a resolution of 60,000 (400 m/z) with a mass range from 350 to 2000 m/z. Tandem mass spectra of the 20 highest abundant precursors were acquired in the linear ion trap after fragmentation by collision-induced dissociation.

Peptide identification was carried out using Proteome Discoverer 1.4 (Thermo Scientific, Bremen, Germany). The acquired spectra were searched against the UniProt reference proteome for *Rattus norvegicus* (UP000002494, release 2015_11, 29880 entries) and UniProt/TrEMBL sequences for *Rat cytomegalovirus* (RCMV-E, isolate England; release 2015_11, 208 entries) using Mascot (v.2.5; Matrix Science, London, UK). Trypsin was set as digesting enzyme and one missed cleavage site was considered as well as dynamic oxidation of methionine and static carbamidomethylation of cysteine residues. The mass tolerance was set to 5 ppm for precursor ions and 0.4 Da for fragment ions. The false discovery rate (FDR) was calculated using the percolator function and only identifications passing an FDR threshold of 1% were considered. Label-free quantification was carried out using Progenesis QI for Proteomics (ver.2.0.5, Nonlinear Dynamics, Newcastle upon Tyne, UK) and the peptide spectrum matches derived from Proteome Discoverer were used for protein identification. Normalised protein abundancies were exported and further processed using R (R Foundation for Statistical Computing, Vienna, Austria). Statistical significance was calculated using acrsinh-transformed data by ANOVA followed by Tukey's honest significant difference method. Ratios of means were calculated using non-transformed data. Proteins passing an ANOVA p_{FDR} value ≤ 0.05 (adjusted according to Benjamini-Hochberg), a post hoc test p value ≤ 0.05 and an absolute ratio of means ≥ 2 were considered as significantly differentially abundant.

Immunoblotting

Immunoblotting was performed according to standard procedures. Briefly, cells were lysed as described (Trilling et al., 2009) and equal amounts of protein were subjected to SDS-PAGE and transferred to nitrocellulose membranes. Immunoblot analysis was performed using the specific antibodies recognizing the indicated proteins (Table S3). Proteins were visualised using peroxidase-coupled secondary antibodies (Dianova) and the ECL chemiluminescence system (Cell Signaling).

Co-immunoprecipitation

Transfected HEK293T cells were washed with ice cold PBS and subsequently lysed as described (Le et al., 2011; Trilling et al., 2011) by incubation for 1h on ice in the following buffer: 0.1 mM EDTA, 150 mM NaCl, 10 mM KCl, 10 mM MgCl2, 10% (v/v) glycerol, 20 mM HEPES (pH 7.4), 0.5% (v/v) NP-40, 0.1 mM PMSF, 1 mM DTT, 10 µM pepstatin A, 5 µM leupeptin, 0.1 mM Na-vanadate, Complete protease inhibitor (Roche). Lysates were cleared by centrifugation for 30 min at 4°C and 16,000 g. The IP antibody (Table S3) was added to the supernatant and incubated overnight at 4°C in a rotating device. Immune complexes were precipitated with Protein-G-Sepharose (GE Healthcare) for 1 h at 4°C in a rotating device and washed with 150, 250, and 400 mM NaCl-containing lysis buffer. Samples were separated by SDS-PAGE for immunoblot analysis of indicated proteins.

Luciferase assays

NIH3T3 reporter cells were infected with MCMV, treated with IFNβ or IFNλ for 6 h, and lysed for quantification of reporter gene expression (Le-Trilling et al., 2018). Luciferase activity was measured according to the manufacturer's instructions (pjk) using a microplate multireader (Mithras2 LB 943; Berthold Technologies). Quantification of luminescence was performed by use of the microplate multireader Mithras2 LB 943 and MicroWin software (Berthold Technologies). The resulting data were analyzed using GraphPad Prism software. The values are reported as Mean ± standard deviation (SD) as described in the figure legends.

Protein production and purification

Constructs in the pHisSUMO vector, containing an N-terminal HisSUMO-tag, followed by a 3C protease cleavage site, were expressed in *Escherichia coli* Rosetta™ 2(DE3). In a typical expression, 2 L LB medium containing 100 µg/mL Ampicillin and 34 µg/mL Chloramphenicol were inoculated with 20 mL of an overnight culture and grown under shaking in an Multitron HT incubator (Infors) at 37°C, 150 rpm, until OD_{600}=0.7. Then, temperature was lowered to 18°C and protein expression was induced by addition of 0.2 mM Isopropyl β-d-1-thiogalactopyranoside (IPTG). Cultures were grown for further 20 h. Bacteria were pelleted by centrifugation at 4000 rpm, 4°C for 15 min using a JLA-9.1000 centrifuge rotor (Beckman). The pellet was resuspended in 70 mL buffer containing 50 mM Tris-HCl, pH 7.8, 500 mM NaCl, 4 mM $MgCl_2$, 0.5 mM tris-(2-carboxyethyl)-phosphine (TCEP), mini-complete protease inhibitors (1 tablet per 50 mL) (Merck), and 30 mM imidazole. 5 µL Benzonase (Merck) was added and the suspension was stirred thoroughly. Cells were lysed by passing the suspension at least twice through a Microfluidiser (Microfluidics). The lysate was clarified by centrifugation at 48000×g for 45 min at 4°C using a JA-25.50 rotor (Beckman), and applied on a XK 16/20 chromatography column (Cytiva) containing 10 mL Ni Sepharose® High Performance beads (Cytiva), using an Äkta pure FPLC (Cytiva) at 4°C. The column was washed with 250 ml buffer containing 50 mM Tris-HCl, pH 7.8, 500 mM NaCl, 4 mM $MgCl_2$, 0.5 mM TCEP, and 30 mM imidazole. Protein was eluted with the same buffer supplemented with 0.3 M imidazole. Eluent fractions were analysed using SDS-PAGE, appropriate fractions were pooled and concentrated to 5 mL with centrifugal filter devices (Vivaspin 20,

Sartorius). In pHisSUMO-rnSTAT2 preparations, 30 µg 3C protease per mg total protein was added and the sample was incubated for 12 h on ice to cleave off the HisSUMO-tag. In pHisSUMO-E27 purifications, the tag was not removed, because tag-free E27 precipitated out of solution at higher concentration in the absence of additional binding partners. Subsequently, gel filtration chromatography (GF) was performed on an Äkta prime plus FPLC (Cytiva), using a Superdex 200 16/600 column (Cytiva), equilibrated in 10 mM Tris-HCl pH 7.8, 150 mM NaCl, 4 mM $MgCl_2$, 0.5 mM TCEP buffer, at a flow rate of 1 mL/min. GF fractions were analysed by SDS-PAGE, appropriate fractions were pooled and concentrated to approx. 20 mg/mL, flash-frozen in liquid nitrogen in small aliquots and stored at -80°C. Protein concentration was determined with a NanoDrop spectrophotometer (ND 1000, Peqlab), using theoretical absorption coefficients calculated based upon the amino acid sequence by ProtParam on the ExPASy webserver (Wilkins et al., 1999).

Constructs in the pAcGHLT-B vector, encoding an N-terminal GST-His-tag, followed by a 3C protease cleavage site, were expressed by infecting Sf9 cells with recombinant baculoviruses (*Autographa californica nucleopolyhedrovirus* clone C6), which were generated as described previously (Zhao et al., 2003). Sf9 cells were cultivated in Insect-XPRESS medium (Lonza) at 28°C, 180 rpm in an Innova 42R incubator shaker (New Brunswick). 1 L Sf9 cells at a cell density of 3×10^6 cells/mL were infected with 0.5 mL of high titre recombinant baculovirus for 72 h. Cells were pelleted by centrifugation at 1000 rpm, 4°C for 30 min using a JLA-9.1000 centrifuge rotor (Beckman). The pellet was resuspended in 500 mL hypotonic lysis buffer containing 10 mM Tris-HCl pH 7.8, 4 mM $MgCl_2$, 30 mM imidazole, 0.5 mM TCEP, mini-complete protease inhibitors (10 tablets) (Merck) and stirred at 4°C for 30 min. The lysate was cleared by centrifugation at 4000×g, 4°C for 30 min. Subsequent purification steps were performed as described above for proteins expressed in *E. coli*.

Analytical gel filtration (GF)

10 µM of each protein component was incubated with 30 µg 3C protease in a volume of 150 µL buffer containing 50 mM Tris-HCl, pH 7.8, 500 mM NaCl, 4 mM $MgCl_2$, and 0.5 mM TCEP, for 12 h on ice. To remove the cleaved purification tags and GST-tagged 3C protease, 20 µL GSH-Sepharose FF beads (Cytiva) were added and the sample was rotated at 4 °C for 1 h. GSH-Sepharose beads were removed by centrifugation at 4°C, 4000 rpm for 5 min, and 120 µL of the supernatant was loaded on an analytical GF column (Superdex 200 Increase 10/300 GL, Cytiva), equilibrated in 10 mM Tris-HCl pH 7.8, 150 mM NaCl, 4 mM $MgCl_2$, and 0.5 mM TCEP, at a flow rate of 0.5 mL/min, using an Äkta pure FPLC (Cytiva). 1 mL fractions were collected and analysed by SDS-PAGE.

Cryo-EM sample preparation

7 µM HisSUMO-E27, 7 µM GST-DDB1$_{\Delta BPB}$, and 7 µM rnSTAT2 were incubated with 0.5 mg 3C protease in a volume of 1 mL buffer containing 10 mM HEPES-NaOH pH 7.8, 150 mM NaCl, 4 mM $MgCl_2$, 0.5 mM TCEP, for 12 h on ice. Subsequently, the sample was subjected to GF chromatography on an Äkta prime plus FPLC (Cytiva), using a Superdex 200 16/600 column (Cytiva), connected in line

to a 1 mL Glutathione Sepharose® 4 Fast Flow column (Cytiva), at a flow rate of 1 mL/min, using the same buffer as eluent. GF fractions were analysed by SDS-PAGE. Fractions corresponding to the elution peak containing E27, $DDB1_{\Delta BPB}$ and rnSTAT2 were pooled and concentrated to 70 µL (protein concentration 4.1 mg/mL).

Suberic acid bis(N-hydroxysuccinimide ester) (DSS) cross-linker (Merck) was added 1:1 (w/w) from a 100 µg/mL stock solution in DMSO, and the sample volume was adjusted to 400 µL with buffer containing 10 mM HEPES-NaOH pH 7.8, 150 mM NaCl, 4 mM $MgCl_2$, 0.5 mM TCEP. The sample was incubated for 1 h at 22°C, and the cross-linking reaction was quenched by the addition of 20 µL 1 M Tris-HCl pH 7.8 for 10 min at 22°C. Precipitate was removed by centrifugation at 16.000×g, 22°C for 5 min. The supernatant was loaded on a Superdex 200 Increase 10/300 GL GF column, equilibrated in 10 mM Tris-HCl pH 7.8, 150 mM NaCl, 4 mM $MgCl_2$, and 0.5 mM TCEP, at a flow rate of 0.5 mL/min, using an Äkta pure FPLC (Cytiva). 0.5 mL fractions were collected and analysed by SDS-PAGE. Fractions containing the cross-linked $DDB1_{\Delta BPB}$/E27/STAT2 complex were pooled, concentrated to 1.3 mg/mL, flash-frozen in 5 µL aliquots in liquid nitrogen and stored at -80°C.

R1.2/1.3 400 mesh Cu holey carbon grids (Quantifoil) were glow-discharged for 30 s using a Harrick plasma cleaner with technical air at 0.3 mbar and 7 W. 3.5 µL solution containing 0.5 µM (0.13 mg/mL) cross-linked $DDB1_{\Delta BPB}$/E27/STAT2 complex were applied to the grid, incubated for 45 s, blotted with a Vitrobot Mark IV device (Thermo Fisher) for 1-2 s at 4°C and 99% humidity, and plunged in liquid ethane. Grids were stored in liquid nitrogen until imaging.

Cryo-EM data collection and processing

Data was collected on a 300 kV Tecnai Polara cryo-EM (Thermo Fisher) equipped with a K2 Summit direct electron detector (Gatan) in super-resolution mode, at a nominal magnification of 31000×, with a pixel size of 0.63 Å/px and the following parameters: defocus range of -1 to -2.5 µm, 50 frames per movie, 200 ms exposure per frame, electron dose of 6.2 e/Å^2/s, leading to a total dose of 62 e/Å^2 per movie. In four independent sessions, data from four grids were collected using Leginon (Suloway et al., 2005) yielding 8.069 movie stacks. Movies were aligned and dose-weighted using MotionCor2 (Zheng et al., 2017). Initial estimation of the contrast transfer function (CTF) was performed with the CTFFind4 package via the Relion 3.0.7 GUI (Mindell and Grigorieff, 2003; Scheres, 2012; Zivanov et al., 2018). Power spectra were manually inspected to remove ice contamination and astigmatic, weak, or poorly defined spectra. Particles were picked using Gautomatch 0.53 (https://www2.mrc-lmb.cam.ac.uk/research/locally-developed-software/zhang-software/) or the Relion 3.0.7 autopicker as indicated in Fig. S3. All subsequent image processing procedures were performed using Relion 3.0.7 or cryoSPARC 3.1 (Punjani and Fleet, 2021; Punjani et al., 2017; Punjani et al., 2020), and are shown in Fig. S3.

Model building and refinement

Guided by the cryo-EM density map 1 (Fig. S3) and CLMS distance restraints (Fig. 2C), a partial molecular model of E27 was generated *de novo* using the program Coot 0.9.5 (Emsley and Cowtan, 2004; Emsley et al., 2010). In addition, *in silico* AlphaFold2 structure prediction of E27 was performed (Jumper et al., 2021) using the ColabFold web server (https://colab.research.google.com/github/sokrypton/ColabFold/blob/main/AlphaFold2.ipynb) (Mirdita et al., 2021). The AlphaFold2 output coordinates were in very good agreement with the experimentally determined E27 structure (RMSD of 1.489 Å, 2764 aligned atoms). Accordingly, the model was completed by merging the initial model with the AlphaFold2 template and adjusting backbone and side chain positions where necessary using Coot 0.9.5. DDB1 coordinates were taken from a previously solved DDB1/DCAF1-CtD complex structure (Banchenko et al., 2021), rigid body-fitted and adjusted manually using Coot 0.9.5. The coordinates of the rnSTAT2 CCD were extracted from the AlphaFold protein structure database (https://alphafold.ebi.ac.uk/entry/Q5XI26) (Varadi et al., 2022), rigid body-fitted and adjusted manually using Coot 0.9.5. As final step, automated real space refinement was performed using the program Phenix 1.19.2-4158 (Liebschner et al., 2019). The refined DDB1/E27/STAT2 CCD structure was then fitted as rigid body in cryo-EM density map 2 (Fig. S3). Full-length rnSTAT2 coordinates (https://alphafold.ebi.ac.uk/entry/Q5XI26) were placed by structural superposition of the CCDs. The STAT2 NTD and TAD were removed, because they could not be assigned to the experimental density, indicating that they are flexibly attached and mobile relative to the other STAT2 domains. Lastly, a chain break was introduced between STAT2 residues 315 and 317, and the STAT2 portion encompassing residues 317-701 (DBD, LD, SH2) was once more separately fitted as rigid body, to account for a small movement relative to the CCD.

Cross-linking mass spectrometry

Photo-Crosslinking

The cross-linker sulfo-SDA (sulfosuccinimidyl 4,4′-azipentanoate) (Thermo Scientific) was dissolved in cross-linking buffer (10 mM HEPES-NaOH, pH 7.8, 150 mM NaCl, 4 mM MgCl, 0.5 mM TCEP) to 100 mM before use. The labelling step was performed by incubating 23 µg aliquots of the $DDB1_{\Delta BPB}$/E27/DDA1/STAT2 complex at 1 mg/mL with 0.2, 0.3, 0.6 and 0.8 mM sulfo-SDA, added, respectively, for an hour. The samples were then irradiated with UV light at 365 nm using a Luxigen LZ1 LED emitter (Osram Sylvania Inc.), to form cross-links, for 10 seconds and quenched with 50 mM Tris.HCl pH 7.5 for 20 min. All steps were performed on ice. Reaction products were separated on a Novex Bis-Tris 4–12% SDS−PAGE gel (Life Technologies) in order to identify suitable cross-linker concentrations. Samples corresponding to 0.2 and 0.3 mM SDA concentrations were precipitated in 80% acetone at -20 °C. All subsequent steps were carried out at room temperature. Protein pellets were resuspended in denaturing buffer (50 mM NH_4HCO_3, 8 M urea), reduced with 2 mM DTT for 30 minutes and alkylated with 5 mM iodoacetamide for 30 minutes. Urea concentration was then reduced to 1.5 M by dilution with 50 mM NH_4HCO_3 and samples were digested with trypsin (Thermo Scientific Pierce)

(Shevchenko et al., 2006) overnight. The resulting tryptic peptides were extracted, desalted using C18 StageTips (Rappsilber et al., 2003) and pooled. Eluted peptides were fractionated on a Superdex Peptide 3.2/300 increase column (GE Healthcare) at a flow rate of 10 µL/min using 30% (v/v) acetonitrile and 0.1 % (v/v) trifluoroacetic acid as mobile phase. 50 µL fractions were collected and vacuum-dried.

CLMS acquisition

Samples for analysis were resuspended in 0.1% (v/v) formic acid, 3.2% (v/v) acetonitrile. LC-MS/MS analysis was performed on an Orbitrap Fusion Lumos Tribrid mass spectrometer (Thermo Fisher) coupled on-line with an Ultimate 3000 RSLCnano HPLC system (Dionex, Thermo Fisher). Samples were separated on a 50 cm EASY-Spray column (Thermo Fisher). Mobile phase A consisted of 0.1% (v/v) formic acid and mobile phase B of 80% (v/v) acetonitrile with 0.1% (v/v) formic acid. Flow rates were 0.3 µL/min using gradients optimised for each chromatographic fraction from offline fractionation, ranging from 2% mobile phase B to 55% mobile phase B over 90 min. MS data were acquired in data-dependent mode using the top-speed setting with a 2.5 s cycle time. For every cycle, the full scan mass spectrum was recorded using the Orbitrap at a resolution of 120,000 in the range of 400 to 1,500 m/z. Ions with a precursor charge state between 3+ and 7+ were isolated and fragmented. Analyte fragmentation was achieved by stepped Higher-Energy Collisional Dissociation (HCD) and a decision tree strategy (Kolbowski et al., 2017). Fragmentation spectra were then recorded in the Orbitrap with a resolution of 60,000. Dynamic exclusion was enabled with single repeat count and 60 s exclusion duration.

CLMS processing

A recalibration of the precursor m/z was conducted based on high-confidence (<1% false discovery rate (FDR)) linear peptide identifications. The re-calibrated peak lists were searched against the sequences and the reversed sequences (as decoys) of cross-linked peptides using the Xi software suite (v.1.7.6.3) for identification (Mendes et al., 2019). Final crosslink lists were compiled using the identified candidates filtered to <2% FDR on link level with xiFDR v.2.1.5.5 (Fischer and Rappsilber, 2017) imposing a minimum of 5 observed fragments per peptide and at least one crosslinker-containing fragment. FDR settings were optimised by boosting heteromeric crosslinks based on delta score, minimum fragments and minimum sequence coverage, and lower result levels.

DisVis

Center of mass position of the DDA1 C-terminal region relative to the complex was determined using DisVis (van Zundert and Bonvin, 2015; van Zundert et al., 2017). The DDB1/STAT2/E27 complex structure from this study was selected as the fixed chain and residues 49-76 of DDA1 from PDB 6ue5 (Bussiere et al., 2020) were selected as the scanning chain. 46 SDA crosslinking restraints were entered from Cα to Cα with allowed distance between 2.5 Å and 22 Å. The rotational sampling was set to 15°.

Sequence alignments

Sequence alignments were calculated using the EBI ClustalOmega server (Madeira et al., 2019) (https://www.ebi.ac.uk/Tools/msa/clustalo/), and adjusted manually using the program GeneDoc (Nicholas, 1997).

Virus taxonomy IDs (TaxID)

HCMV, 10359; MuHV-1, 10366; MuHV-2, 79700; MuHV-8, 1261657

Amino acid sequences used for multiple sequence alignments

E27, NCBI YP_007016432; M27, NCBI AWV68118; R27, NCBI NP_064132; T27, NCBI NP_116370; B27, NCBI AFK83839; rhesus macaque UL27 (RH27), NCBI AAZ80544; UL27, NCBI ACN63126; DCAF1, UniProt Q9Y4B6; DCAF2, UniProt Q9NZJ0; DCAF4, UniProt Q8WV16; DCAF5, UniProt Q96JK2; DCAF6, UniProt Q58WW2; DCAF8, UniProt Q5TAQ9; DCAF9, UniProt Q8N5D0; DCAF10, UniProt Q5QP82; DCAF11, UniProt Q8TEB1; DCAF12, UniProt Q5T6F0; DCAF14, UniProt Q8WWQ0; DCAF15, UniProt Q66K64; DCAF17, UniProt Q5H9S7; AMBRA1, UniProt Q9C0C7; CSA, UniProt Q13216; DDB2, UniProt Q92466; HBX, NCBI AMH41022; WHX, NCBI AAA46776; SV5V, UniProt P11207; UL145, UniProt F5HF44; rat STAT2, UniProt Q5XI26; mouse STAT2, UniProt Q9WVL2; human STAT2, UniProt P52630; rhesus macaque STAT2, UniProt F6R1P6; pig STAT2, UniProt O02799; chicken STAT2, UniProt A0A1D5PIV4; frog STAT2, UniProt A0A1L8HHX5

Data availability

LC-MS data have been deposited at ProteomeXchange via the PRIDE partner repository (Perez-Riverol et al., 2019) with the dataset identifier PXD033639 (reviewer account username: reviewer_pxd033639@ebi.ac.uk, password: KsIRcYHZ). CLMS data have been deposited at the JPOST ProteomeXChange (Deutsch et al., 2020) with accession number JPST001566 (ProteomeXChange PXD033366, reviewer details: https://repository.jpostdb.org/preview/110121477262651feae5f48, access key: 3943). The EM maps have been deposited at the Electron Microscopy Data Bank (EMDB) with the accession numbers EMD-14802 (map 1) and EMD-14812 (map 2). Atom coordinates have been deposited at the Protein Data Bank (PDB) with the accession numbers 7zn7 ($DDB1_{\Delta BPB}$/E27/STAT2 CCD) and 7znn ($DDB1_{\Delta BPB}$/E27/STAT2 FL).

Supplementary Information

Figure S1: Proteomic analysis of protein abundance changes upon RCMV-E infection

(A) Mass spectrometric analysis of protein abundance changes upon RCMV-E infection, compared to mock-infected samples, at indicated time points. Significantly down- or upregulated proteins are marked red.

(B) Relative abundance changes of selected proteins involved in IFN-signalling upon RCMV-E infection, compared to mock-infected samples, at indicated time points.

Figure S2: Cryo-EM sample preparation

(A) GF chromatogram of the disuccinimidyl suberate (DSS) cross-linked $DDB1_{\Delta BPB}$/DDA1/E27/STAT2 protein complex. GF fractions, which have been pooled for cryo-EM analysis are indicated.

(B) SDS-PAGE analysis of the cross-linking reaction and GF fractions.

Figure S3: Cryo-EM data processing flowchart

If not stated otherwise, all computational procedures have been performed using the program Relion 3.0.7 (Zivanov et al., 2018).

Figure S4: Confidence scores AlphaFold2 predictions and multiple sequence alignment of E27 and its homologs

(A) Cartoon representation of the E27 and M27 AlphaFold2 models, coloured according to model confidence, i.e., the model's prediction of its score on the local Distance Difference Test (lDDT-Cα) (Jumper et al., 2021). Terminal regions with very low confidence have been removed from the models for clarity.

(B) Multiple sequence alignment of E27 and its homologs from other CMV species. Secondary structure elements are drawn schematically above the alignment. Dashed lines indicate flexible regions not included in the molecular model. Residues involved in DDB1-binding and in the main STAT2-binding interface are indicated by blue and magenta dots above the alignment, respectively. Residue stretches involved in the auxiliary E27 α/β-domain/STAT2 DBD binding interface are indicated by magenta lines above the alignment. Side chains involved in zinc-coordination are marked by grey dots.

(C) Cartoon representation of the HBx AlphaFold2 model, coloured as in **A**. Terminal regions with very low confidence have been removed.

Figure S5: Molecular modelling of DDA1

(A) Superposition of a $DDB1_{\Delta BPB}$/DDA1/DCAF15 complex structure (PDB 6q0v) (Faust et al., 2020) with the $DDB1_{\Delta BPB}$/E27 complex coordinates. Proteins are shown as cartoons, DDB1 is coloured blue, E27 green and DDA1 red. DCAF15 has been removed for clarity, and only DDB1 from the DDB1/E27

structure is shown. DDA1 termini and the C-terminal helix are indicated. Experimental cryo-EM map 1 is shown as semi-transparent surface.

(B) Visualisation (grey semi-transparent surface) of the space accessible to the centre of mass of the DDA1 C-terminal helix, calculated based on cross-link distance restraints, consistent with at least 15 of the observed cross-links involving DDA1, using the DisVis software tool (van Zundert and Bonvin, 2015; van Zundert et al., 2017). Proteins are represented as in **A**. This analysis implies that the C-terminal helix preferentially locates to a relatively large area around the edges of DDB1 BPC and CTD, and does not occupy a defined location in contact with E27, as observed in the $DDB1_{\Delta BPB}$/DDA1/DCAF15 complex (indicated by the red arrow).

Figure S6: CLMS analysis of DDB1/E27/STAT2 models derived from cryo-EM map 1 and map 2

(**A**) Left panel: sulfo-SDA cross-links mapped onto the DDB1/E27/STAT2 model built in map 1. Both within protein and heteromeric links are displayed. Satisfied cross-links (shorter than 25 Å Cα-Cα) are coloured in blue, moderate violations (25-35 Å) in orange and violated (> 35 Å) cross-links in red. Right panel: circle view of the links between proteins colored by cross-link satisfaction. Grey cross-links lie between regions not modelled in the structure. Solid coloured bars indicate structural coverage.

(**B**) As in **A**, but for the model built in map 2. Violated cross-links between E27 α/β-domain, STAT2 and DDB1 may indicate a swivel motion of the top of the complex relative to DDB1, which is consistent with the high mobility of this module relative to the core of the complex observed in cryo-EM analysis.

Table S1: Cryo-EM data collection and refinement

Table S2: Crosslink violation analysis

Table S3: Key resources

Table S4: Oligonucleotide primer sequences

References

Angers, S., Li, T., Yi, X., MacCoss, M.J., Moon, R.T., and Zheng, N. (2006). Molecular architecture and assembly of the DDB1-CUL4A ubiquitin ligase machinery. Nature *443*, 590-593.

Ashour, J., Laurent-Rolle, M., Shi, P.Y., and Garcia-Sastre, A. (2009). NS5 of dengue virus mediates STAT2 binding and degradation. Journal of virology *83*, 5408-5418.

Baek, K., Krist, D.T., Prabu, J.R., Hill, S., Klugel, M., Neumaier, L.M., von Gronau, S., Kleiger, G., and Schulman, B.A. (2020). NEDD8 nucleates a multivalent cullin-RING-UBE2D ubiquitin ligation assembly. Nature *578*, 461-466.

Banchenko, S., Krupp, F., Gotthold, C., Burger, J., Graziadei, A., O'Reilly, F.J., Sinn, L., Ruda, O., Rappsilber, J., Spahn, C.M.T.*, et al.* (2021). Structural insights into Cullin4-RING ubiquitin ligase remodelling by Vpr from simian immunodeficiency viruses. PLoS pathogens *17*, e1009775.

Baranek, T., Manh, T.P., Alexandre, Y., Maqbool, M.A., Cabeza, J.Z., Tomasello, E., Crozat, K., Bessou, G., Zucchini, N., Robbins, S.H.*, et al.* (2012). Differential responses of immune cells to type I interferon contribute to host resistance to viral infection. Cell host & microbe *12*, 571-584.

Barik, S. (2022). Mechanisms of Viral Degradation of Cellular Signal Transducer and Activator of Transcription 2. Int J Mol Sci *23*.

Becker, S.D., Bennett, M., Stewart, J.P., and Hurst, J.L. (2007). Serological survey of virus infection among wild house mice (Mus domesticus) in the UK. Lab Anim *41*, 229-238.

Becker, T., Le-Trilling, V.T.K., and Trilling, M. (2019). Cellular Cullin RING Ubiquitin Ligases: Druggable Host Dependency Factors of Cytomegaloviruses. Int J Mol Sci *20*.

Blaszczyk, K., Olejnik, A., Nowicka, H., Ozgyin, L., Chen, Y.L., Chmielewski, S., Kostyrko, K., Wesoly, J., Balint, B.L., Lee, C.K.*, et al.* (2015). STAT2/IRF9 directs a prolonged ISGF3-like transcriptional response and antiviral activity in the absence of STAT1. Biochem J *466*, 511-524.

Brizic, I., Lisnic, B., Brune, W., Hengel, H., and Jonjic, S. (2018). Cytomegalovirus Infection: Mouse Model. Curr Protoc Immunol *122*, e51.

Bussiere, D.E., Xie, L., Srinivas, H., Shu, W., Burke, A., Be, C., Zhao, J., Godbole, A., King, D., Karki, R.G.*, et al.* (2020). Structural basis of indisulam-mediated RBM39 recruitment to DCAF15 E3 ligase complex. Nat Chem Biol *16*, 15-23.

Cavadini, S., Fischer, E.S., Bunker, R.D., Potenza, A., Lingaraju, G.M., Goldie, K.N., Mohamed, W.I., Faty, M., Petzold, G., Beckwith, R.E.*, et al.* (2016). Cullin-RING ubiquitin E3 ligase regulation by the COP9 signalosome. Nature *531*, 598-603.

Darnell, J.E., Jr., Kerr, I.M., and Stark, G.R. (1994). Jak-STAT pathways and transcriptional activation in response to IFNs and other extracellular signaling proteins. Science *264*, 1415-1421.

Decorsiere, A., Mueller, H., van Breugel, P.C., Abdul, F., Gerossier, L., Beran, R.K., Livingston, C.M., Niu, C., Fletcher, S.P., Hantz, O.*, et al.* (2016). Hepatitis B virus X protein identifies the Smc5/6 complex as a host restriction factor. Nature *531*, 386-389.

Deutsch, E.W., Bandeira, N., Sharma, V., Perez-Riverol, Y., Carver, J.J., Kundu, D.J., Garcia-Seisdedos, D., Jarnuczak, A.F., Hewapathirana, S., Pullman, B.S.*, et al.* (2020). The ProteomeXchange consortium in 2020: enabling 'big data' approaches in proteomics. Nucleic acids research *48*, D1145-D1152.

Du, X., Volkov, O.A., Czerwinski, R.M., Tan, H., Huerta, C., Morton, E.R., Rizzi, J.P., Wehn, P.M., Xu, R., Nijhawan, D., *et al.* (2019). Structural Basis and Kinetic Pathway of RBM39 Recruitment to DCAF15 by a Sulfonamide Molecular Glue E7820. Structure *27*, 1625-1633 e1623.

Emsley, P., and Cowtan, K. (2004). Coot: model-building tools for molecular graphics. Acta crystallographica Section D, Biological crystallography *60*, 2126-2132.

Emsley, P., Lohkamp, B., Scott, W.G., and Cowtan, K. (2010). Features and development of Coot. Acta crystallographica Section D, Biological crystallography *66*, 486-501.

Ettinger, J., Geyer, H., Nitsche, A., Zimmermann, A., Brune, W., Sandford, G.R., Hayward, G.S., and Voigt, S. (2012). Complete genome sequence of the english isolate of rat cytomegalovirus (Murid herpesvirus 8). Journal of virology *86*, 13838.

Faust, T.B., Yoon, H., Nowak, R.P., Donovan, K.A., Li, Z., Cai, Q., Eleuteri, N.A., Zhang, T., Gray, N.S., and Fischer, E.S. (2020). Structural complementarity facilitates E7820-mediated degradation of RBM39 by DCAF15. Nat Chem Biol *16*, 7-14.

Fischer, E.S., Bohm, K., Lydeard, J.R., Yang, H., Stadler, M.B., Cavadini, S., Nagel, J., Serluca, F., Acker, V., Lingaraju, G.M., *et al.* (2014). Structure of the DDB1-CRBN E3 ubiquitin ligase in complex with thalidomide. Nature *512*, 49-53.

Fischer, E.S., Scrima, A., Bohm, K., Matsumoto, S., Lingaraju, G.M., Faty, M., Yasuda, T., Cavadini, S., Wakasugi, M., Hanaoka, F., *et al.* (2011). The molecular basis of CRL4DDB2/CSA ubiquitin ligase architecture, targeting, and activation. Cell *147*, 1024-1039.

Geyer, H., Ettinger, J., Moller, L., Schmolz, E., Nitsche, A., Brune, W., Heaggans, S., Sandford, G.R., Hayward, G.S., and Voigt, S. (2015). Rat cytomegalovirus (RCMV) English isolate and a newly identified Berlin isolate share similarities with but are separate as an anciently diverged clade from Mouse CMV and the Maastricht isolate of RCMV. The Journal of general virology *96*, 1873-1870.

Goldenberg, S.J., Cascio, T.C., Shumway, S.D., Garbutt, K.C., Liu, J., Xiong, Y., and Zheng, N. (2004). Structure of the Cand1-Cul1-Roc1 complex reveals regulatory mechanisms for the assembly of the multisubunit cullin-dependent ubiquitin ligases. Cell *119*, 517-528.

Gowen, B.B., Westover, J.B., Miao, J., Van Wettere, A.J., Rigas, J.D., Hickerson, B.T., Jung, K.H., Li, R., Conrad, B.L., Nielson, S., *et al.* (2017). Modeling Severe Fever with Thrombocytopenia Syndrome Virus Infection in Golden Syrian Hamsters: Importance of STAT2 in Preventing Disease and Effective Treatment with Favipiravir. Journal of virology *91*.

Grant, A., Ponia, S.S., Tripathi, S., Balasubramaniam, V., Miorin, L., Sourisseau, M., Schwarz, M.C., Sanchez-Seco, M.P., Evans, M.J., Best, S.M., *et al.* (2016). Zika Virus Targets Human STAT2 to Inhibit Type I Interferon Signaling. Cell host & microbe *19*, 882-890.

Greenwood, E.J.D., Williamson, J.C., Sienkiewicz, A., Naamati, A., Matheson, N.J., and Lehner, P.J. (2019). Promiscuous Targeting of Cellular Proteins by Vpr Drives Systems-Level Proteomic Remodeling in HIV-1 Infection. Cell reports *27*, 1579-1596 e1577.

Griffiths, P., and Reeves, M. (2021). Pathogenesis of human cytomegalovirus in the immunocompromised host. Nat Rev Microbiol *19*, 759-773.

Hambleton, S., Goodbourn, S., Young, D.F., Dickinson, P., Mohamad, S.M., Valappil, M., McGovern, N., Cant, A.J., Hackett, S.J., Ghazal, P., *et al.* (2013). STAT2 deficiency and susceptibility to viral illness in humans. Proceedings of the National Academy of Sciences of the United States of America *110*, 3053-3058.

Hansson, M.D., Rzeznicka, K., Rosenback, M., Hansson, M., and Sirijovski, N. (2008). PCR-mediated deletion of plasmid DNA. Anal Biochem *375*, 373-375.

Harper, J.W., and Schulman, B.A. (2021). Cullin-RING Ubiquitin Ligase Regulatory Circuits: A Quarter Century Beyond the F-Box Hypothesis. Annual review of biochemistry *90*, 403-429.

Hein, M.Y., and Weissman, J.S. (2021). Functional single-cell genomics of human cytomegalovirus infection. bioRxiv, 775080.

Ho, J., Pelzel, C., Begitt, A., Mee, M., Elsheikha, H.M., Scott, D.J., and Vinkemeier, U. (2016). STAT2 Is a Pervasive Cytokine Regulator due to Its Inhibition of STAT1 in Multiple Signaling Pathways. PLoS Biol *14*, e2000117.

Horvath, C.M., Stark, G.R., Kerr, I.M., and Darnell, J.E., Jr. (1996). Interactions between STAT and non-STAT proteins in the interferon-stimulated gene factor 3 transcription complex. Molecular and cellular biology *16*, 6957-6964.

Humphreys, I.R., Pei, J., Baek, M., Krishnakumar, A., Anishchenko, I., Ovchinnikov, S., Zhang, J., Ness, T.J., Banjade, S., Bagde, S.R.*, et al.* (2021). Computed structures of core eukaryotic protein complexes. Science *374*, eabm4805.

Isaacs, A., and Lindenmann, J. (1957). Virus interference. I. The interferon. Proc R Soc Lond B Biol Sci *147*, 258-267.

Ivashkiv, L.B., and Donlin, L.T. (2014). Regulation of type I interferon responses. Nat Rev Immunol *14*, 36-49.

Jones, M., Davidson, A., Hibbert, L., Gruenwald, P., Schlaak, J., Ball, S., Foster, G.R., and Jacobs, M. (2005). Dengue virus inhibits alpha interferon signaling by reducing STAT2 expression. Journal of virology *79*, 5414-5420.

Jordan, S., Krause, J., Prager, A., Mitrovic, M., Jonjic, S., Koszinowski, U.H., and Adler, B. (2011). Virus progeny of murine cytomegalovirus bacterial artificial chromosome pSM3fr show reduced growth in salivary Glands due to a fixed mutation of MCK-2. Journal of virology *85*, 10346-10353.

Jumper, J., Evans, R., Pritzel, A., Green, T., Figurnov, M., Ronneberger, O., Tunyasuvunakool, K., Bates, R., Zidek, A., Potapenko, A.*, et al.* (2021). Highly accurate protein structure prediction with AlphaFold. Nature *596*, 583-589.

Kotenko, S.V., Gallagher, G., Baurin, V.V., Lewis-Antes, A., Shen, M., Shah, N.K., Langer, J.A., Sheikh, F., Dickensheets, H., and Donnelly, R.P. (2003). IFN-lambdas mediate antiviral protection through a distinct class II cytokine receptor complex. Nature immunology *4*, 69-77.

Landsberg, C.D., Megger, D.A., Hotter, D., Ruckborn, M.U., Eilbrecht, M., Rashidi-Alavijeh, J., Howe, S., Heinrichs, S., Sauter, D., Sitek, B.*, et al.* (2018). A Mass Spectrometry-Based Profiling of Interactomes of Viral DDB1- and Cullin Ubiquitin Ligase-Binding Proteins Reveals NF-kappaB Inhibitory Activity of the HIV-2-Encoded Vpx. Front Immunol *9*, 2978.

Le-Trilling, V.T., Megger, D.A., Katschinski, B., Landsberg, C.D., Ruckborn, M.U., Tao, S., Krawczyk, A., Bayer, W., Drexler, I., Tenbusch, M.*, et al.* (2016). Broad and potent antiviral activity of the NAE inhibitor MLN4924. Scientific reports *6*, 19977.

Le-Trilling, V.T., and Trilling, M. (2017). Mouse newborn cells allow highly productive mouse cytomegalovirus replication, constituting a novel convenient primary cell culture system. PloS one *12*, e0174695.

Le-Trilling, V.T.K., Becker, T., Nachshon, A., Stern-Ginossar, N., Scholer, L., Voigt, S., Hengel, H., and Trilling, M. (2020). The Human Cytomegalovirus pUL145 Isoforms Act as Viral DDB1-Cullin-Associated Factors to Instruct Host Protein Degradation to Impede Innate Immunity. Cell reports *30*, 2248-2260 e2245.

Le-Trilling, V.T.K., and Trilling, M. (2020). Ub to no good: How cytomegaloviruses exploit the ubiquitin proteasome system. Virus Res *281*, 197938.

Le-Trilling, V.T.K., Wohlgemuth, K., Ruckborn, M.U., Jagnjic, A., Maassen, F., Timmer, L., Katschinski, B., and Trilling, M. (2018). STAT2-Dependent Immune Responses Ensure Host Survival despite the Presence of a Potent Viral Antagonist. Journal of virology *92*.

Le, V.T., Trilling, M., and Hengel, H. (2011). The cytomegaloviral protein pUL138 acts as potentiator of tumor necrosis factor (TNF) receptor 1 surface density to enhance ULb'-encoded modulation of TNF-alpha signaling. Journal of virology *85*, 13260-13270.

Le, V.T.K., Trilling, M., Wilborn, M., Hengel, H., and Zimmermann, A. (2008). Human cytomegalovirus interferes with signal transducer and activator of transcription (STAT) 2 protein stability and tyrosine phosphorylation. The Journal of general virology *89*, 2416-2426.

Levy, D.E., and Darnell, J.E., Jr. (2002). Stats: transcriptional control and biological impact. Nature reviews Molecular cell biology *3*, 651-662.

Li, T., Robert, E.I., van Breugel, P.C., Strubin, M., and Zheng, N. (2010). A promiscuous alpha-helical motif anchors viral hijackers and substrate receptors to the CUL4-DDB1 ubiquitin ligase machinery. Nature structural & molecular biology *17*, 105-111.

Liebschner, D., Afonine, P.V., Baker, M.L., Bunkoczi, G., Chen, V.B., Croll, T.I., Hintze, B., Hung, L.W., Jain, S., McCoy, A.J.*, et al.* (2019). Macromolecular structure determination using X-rays, neutrons and electrons: recent developments in Phenix. Acta Crystallogr D Struct Biol *75*, 861-877.

Lin, G.Y., Paterson, R.G., Richardson, C.D., and Lamb, R.A. (1998). The V protein of the paramyxovirus SV5 interacts with damage-specific DNA binding protein. Virology *249*, 189-200.

Madeira, F., Park, Y.M., Lee, J., Buso, N., Gur, T., Madhusoodanan, N., Basutkar, P., Tivey, A.R.N., Potter, S.C., Finn, R.D.*, et al.* (2019). The EMBL-EBI search and sequence analysis tools APIs in 2019. Nucleic acids research *47*, W636-W641.

Matsumoto, M., Tanaka, N., Harada, H., Kimura, T., Yokochi, T., Kitagawa, M., Schindler, C., and Taniguchi, T. (1999). Activation of the transcription factor ISGF3 by interferon-gamma. Biol Chem *380*, 699-703.

Megger, D.A., Philipp, J., Le-Trilling, V.T.K., Sitek, B., and Trilling, M. (2017). Deciphering of the Human Interferon-Regulated Proteome by Mass Spectrometry-Based Quantitative Analysis Reveals Extent and Dynamics of Protein Induction and Repression. Front Immunol *8*, 1139.

Mindell, J.A., and Grigorieff, N. (2003). Accurate determination of local defocus and specimen tilt in electron microscopy. J Struct Biol *142*, 334-347.

Mirdita, M., Ovchinnikov, S., and Steinegger, M. (2021). ColabFold - Making protein folding accessible to all. bioRxiv, 2021.2008.2015.456425.

Nicholas, K.B., Nicholas Jr., H. B., Deerfield II., D. W. (1997). GeneDoc: Analysis and Visualization of Genetic Variation. embnetnews *4*, 1-4.

Nightingale, K., Lin, K.M., Ravenhill, B.J., Davies, C., Nobre, L., Fielding, C.A., Ruckova, E., Fletcher-Etherington, A., Soday, L., Nichols, H., *et al.* (2018). High-Definition Analysis of Host Protein Stability during Human Cytomegalovirus Infection Reveals Antiviral Factors and Viral Evasion Mechanisms. Cell host & microbe *24*, 447-460 e411.

Nightingale, K., Potts, M., Hunter, L.M., Fielding, C.A., Zerbe, C.M., Fletcher-Etherington, A., Nobre, L., Wang, E.C.Y., Strang, B.L., Houghton, J.W., *et al.* (2022). Human cytomegalovirus protein RL1 degrades the antiviral factor SLFN11 via recruitment of the CRL4 E3 ubiquitin ligase complex. Proceedings of the National Academy of Sciences of the United States of America *119*.

Nobre, L.V., Nightingale, K., Ravenhill, B.J., Antrobus, R., Soday, L., Nichols, J., Davies, J.A., Seirafian, S., Wang, E.C., Davison, A.J., *et al.* (2019). Human cytomegalovirus interactome analysis identifies degradation hubs, domain associations and viral protein functions. Elife *8*.

Olma, M.H., Roy, M., Le Bihan, T., Sumara, I., Maerki, S., Larsen, B., Quadroni, M., Peter, M., Tyers, M., and Pintard, L. (2009). An interaction network of the mammalian COP9 signalosome identifies Dda1 as a core subunit of multiple Cul4-based E3 ligases. Journal of cell science *122*, 1035-1044.

Panne, D., Maniatis, T., and Harrison, S.C. (2007). An atomic model of the interferon-beta enhanceosome. Cell *129*, 1111-1123.

Parisien, J.P., Lau, J.F., Rodriguez, J.J., Sullivan, B.M., Moscona, A., Parks, G.D., Lamb, R.A., and Horvath, C.M. (2001). The V protein of human parainfluenza virus 2 antagonizes type I interferon responses by destabilizing signal transducer and activator of transcription 2. Virology *283*, 230-239.

Parisien, J.P., Lau, J.F., Rodriguez, J.J., Ulane, C.M., and Horvath, C.M. (2002). Selective STAT protein degradation induced by paramyxoviruses requires both STAT1 and STAT2 but is independent of alpha/beta interferon signal transduction. Journal of virology *76*, 4190-4198.

Park, C., Li, S., Cha, E., and Schindler, C. (2000). Immune response in Stat2 knockout mice. Immunity *13*, 795-804.

Perez-Riverol, Y., Csordas, A., Bai, J., Bernal-Llinares, M., Hewapathirana, S., Kundu, D.J., Inuganti, A., Griss, J., Mayer, G., Eisenacher, M., *et al.* (2019). The PRIDE database and related tools and resources in 2019: improving support for quantification data. Nucleic acids research *47*, D442-D450.

Platanitis, E., Demiroz, D., Schneller, A., Fischer, K., Capelle, C., Hartl, M., Gossenreiter, T., Muller, M., Novatchkova, M., and Decker, T. (2019). A molecular switch from STAT2-IRF9 to ISGF3 underlies interferon-induced gene transcription. Nature communications *10*, 2921.

Precious, B., Childs, K., Fitzpatrick-Swallow, V., Goodbourn, S., and Randall, R.E. (2005). Simian virus 5 V protein acts as an adaptor, linking DDB1 to STAT2, to facilitate the ubiquitination of STAT1. Journal of virology *79*, 13434-13441.

Punjani, A., and Fleet, D.J. (2021). 3D variability analysis: Resolving continuous flexibility and discrete heterogeneity from single particle cryo-EM. J Struct Biol *213*, 107702.

Punjani, A., Rubinstein, J.L., Fleet, D.J., and Brubaker, M.A. (2017). cryoSPARC: algorithms for rapid unsupervised cryo-EM structure determination. Nat Methods *14*, 290-296.

Punjani, A., Zhang, H., and Fleet, D.J. (2020). Non-uniform refinement: adaptive regularization improves single-particle cryo-EM reconstruction. Nat Methods *17*, 1214-1221.

Qureshi, S.A., Salditt-Georgieff, M., and Darnell, J.E., Jr. (1995). Tyrosine-phosphorylated Stat1 and Stat2 plus a 48-kDa protein all contact DNA in forming interferon-stimulated-gene factor 3. Proceedings of the National Academy of Sciences of the United States of America *92*, 3829-3833.

Ramakrishnan, D., Xing, W., Beran, R.K., Chemuru, S., Rohrs, H., Niedziela-Majka, A., Marchand, B., Mehra, U., Zabransky, A., Dolezal, M.*, et al.* (2019). Hepatitis B Virus X Protein Function Requires Zinc Binding. Journal of virology *93*.

Rappsilber, J., Ishihama, Y., and Mann, M. (2003). Stop and go extraction tips for matrix-assisted laser desorption/ionization, nanoelectrospray, and LC/MS sample pretreatment in proteomics. Anal Chem *75*, 663-670.

Rattay, S., Trilling, M., Megger, D.A., Sitek, B., Meyer, H.E., Hengel, H., and Le-Trilling, V.T. (2015). The Canonical Immediate Early 3 Gene Product pIE611 of Mouse Cytomegalovirus Is Dispensable for Viral Replication but Mediates Transcriptional and Posttranscriptional Regulation of Viral Gene Products. Journal of virology *89*, 8590-8598.

Reddehase, M.J., and Lemmermann, N.A.W. (2018). Mouse Model of Cytomegalovirus Disease and Immunotherapy in the Immunocompromised Host: Predictions for Medical Translation that Survived the "Test of Time". Viruses *10*.

Reichermeier, K.M., Straube, R., Reitsma, J.M., Sweredoski, M.J., Rose, C.M., Moradian, A., den Besten, W., Hinkle, T., Verschueren, E., Petzold, G.*, et al.* (2020). PIKES Analysis Reveals Response to Degraders and Key Regulatory Mechanisms of the CRL4 Network. Molecular cell *77*, 1092-1106 e1099.

Reitsma, J.M., Savaryn, J.P., Faust, K., Sato, H., Halligan, B.D., and Terhune, S.S. (2011). Antiviral inhibition targeting the HCMV kinase pUL97 requires pUL27-dependent degradation of Tip60 acetyltransferase and cell-cycle arrest. Cell host & microbe *9*, 103-114.

Rengachari, S., Groiss, S., Devos, J.M., Caron, E., Grandvaux, N., and Panne, D. (2018). Structural basis of STAT2 recognition by IRF9 reveals molecular insights into ISGF3 function. Proceedings of the National Academy of Sciences of the United States of America *115*, E601-E609.

Salsman, J., Jagannathan, M., Paladino, P., Chan, P.K., Dellaire, G., Raught, B., and Frappier, L. (2012). Proteomic profiling of the human cytomegalovirus UL35 gene products reveals a role for UL35 in the DNA repair response. Journal of virology *86*, 806-820.

Scheres, S.H. (2012). RELION: implementation of a Bayesian approach to cryo-EM structure determination. J Struct Biol *180*, 519-530.

Schneider, K., Loewendorf, A., De Trez, C., Fulton, J., Rhode, A., Shumway, H., Ha, S., Patterson, G., Pfeffer, K., Nedospasov, S.A.*, et al.* (2008). Lymphotoxin-mediated crosstalk between B cells and splenic stroma promotes the initial type I interferon response to cytomegalovirus. Cell host & microbe *3*, 67-76.

Schwefel, D., Boucherit, V.C., Christodoulou, E., Walker, P.A., Stoye, J.P., Bishop, K.N., and Taylor, I.A. (2015). Molecular Determinants for Recognition of Divergent SAMHD1 Proteins by the Lentiviral Accessory Protein Vpx. Cell host & microbe *17*, 489-499.

Schwefel, D., Groom, H.C., Boucherit, V.C., Christodoulou, E., Walker, P.A., Stoye, J.P., Bishop, K.N., and Taylor, I.A. (2014). Structural basis of lentiviral subversion of a cellular protein degradation pathway. Nature *505*, 234-238.

Shabek, N., Ruble, J., Waston, C.J., Garbutt, K.C., Hinds, T.R., Li, T., and Zheng, N. (2018). Structural insights into DDA1 function as a core component of the CRL4-DDB1 ubiquitin ligase. Cell Discov *4*, 67.

Shevchenko, A., Tomas, H., Havlis, J., Olsen, J.V., and Mann, M. (2006). In-gel digestion for mass spectrometric characterization of proteins and proteomes. Nature protocols *1*, 2856-2860.

Suloway, C., Pulokas, J., Fellmann, D., Cheng, A., Guerra, F., Quispe, J., Stagg, S., Potter, C.S., and Carragher, B. (2005). Automated molecular microscopy: the new Leginon system. J Struct Biol *151*, 41-60.

Tischer, B.K., von Einem, J., Kaufer, B., and Osterrieder, N. (2006). Two-step red-mediated recombination for versatile high-efficiency markerless DNA manipulation in Escherichia coli. Biotechniques *40*, 191-197.

Trilling, M., Bellora, N., Rutkowski, A.J., de Graaf, M., Dickinson, P., Robertson, K., Prazeres da Costa, O., Ghazal, P., Friedel, C.C., Alba, M.M.*, et al.* (2013). Deciphering the modulation of gene expression by type I and II interferons combining 4sU-tagging, translational arrest and in silico promoter analysis. Nucleic acids research *41*, 8107-8125.

Trilling, M., Le, V.T., Fiedler, M., Zimmermann, A., Bleifuss, E., and Hengel, H. (2011). Identification of DNA-damage DNA-binding protein 1 as a conditional essential factor for cytomegalovirus replication in interferon-gamma-stimulated cells. PLoS pathogens *7*, e1002069.

Trilling, M., Le, V.T., Zimmermann, A., Ludwig, H., Pfeffer, K., Sutter, G., Smith, G.L., and Hengel, H. (2009). Gamma interferon-induced interferon regulatory factor 1-dependent antiviral response inhibits vaccinia virus replication in mouse but not human fibroblasts. Journal of virology *83*, 3684-3695.

Ulane, C.M., and Horvath, C.M. (2002). Paramyxoviruses SV5 and HPIV2 assemble STAT protein ubiquitin ligase complexes from cellular components. Virology *304*, 160-166.

Ulane, C.M., Kentsis, A., Cruz, C.D., Parisien, J.P., Schneider, K.L., and Horvath, C.M. (2005). Composition and assembly of STAT-targeting ubiquitin ligase complexes: paramyxovirus V protein carboxyl terminus is an oligomerization domain. Journal of virology *79*, 10180-10189.

van Diemen, F.R., Kruse, E.M., Hooykaas, M.J., Bruggeling, C.E., Schurch, A.C., van Ham, P.M., Imhof, S.M., Nijhuis, M., Wiertz, E.J., and Lebbink, R.J. (2016). CRISPR/Cas9-Mediated Genome Editing of Herpesviruses Limits Productive and Latent Infections. PLoS pathogens *12*, e1005701.

van Zundert, G.C., and Bonvin, A.M. (2015). DisVis: quantifying and visualizing accessible interaction space of distance-restrained biomolecular complexes. Bioinformatics *31*, 3222-3224.

van Zundert, G.C., Trellet, M., Schaarschmidt, J., Kurkcuoglu, Z., David, M., Verlato, M., Rosato, A., and Bonvin, A.M. (2017). The DisVis and PowerFit Web Servers: Explorative and Integrative Modeling of Biomolecular Complexes. Journal of molecular biology *429*, 399-407.

Varadi, M., Anyango, S., Deshpande, M., Nair, S., Natassia, C., Yordanova, G., Yuan, D., Stroe, O., Wood, G., Laydon, A.*, et al.* (2022). AlphaFold Protein Structure Database: massively expanding the structural coverage of protein-sequence space with high-accuracy models. Nucleic acids research *50*, D439-D444.

Virgin, H.W., Wherry, E.J., and Ahmed, R. (2009). Redefining chronic viral infection. Cell *138*, 30-50.

Voigt, S., Mesci, A., Ettinger, J., Fine, J.H., Chen, P., Chou, W., and Carlyle, J.R. (2007). Cytomegalovirus evasion of innate immunity by subversion of the NKR-P1B:Clr-b missing-self axis. Immunity *26*, 617-627.

Wagner, M., Ruzsics, Z., and Koszinowski, U.H. (2002). Herpesvirus genetics has come of age. Trends Microbiol *10*, 318-324.

Wang, H., Guo, H., Su, J., Rui, Y., Zheng, W., Gao, W., Zhang, W., Li, Z., Liu, G., Markham, R.B.*, et al.* (2017). Inhibition of Vpx-Mediated SAMHD1 and Vpr-Mediated Host Helicase Transcription Factor Degradation by Selective Disruption of Viral CRL4 (DCAF1) E3 Ubiquitin Ligase Assembly. Journal of virology *91*.

Wilkins, M.R., Gasteiger, E., Bairoch, A., Sanchez, J.C., Williams, K.L., Appel, R.D., and Hochstrasser, D.F. (1999). Protein identification and analysis tools in the ExPASy server. Methods Mol Biol *112*, 531-552.

Yamamoto, M., Koga, R., Fujino, H., Shimagaki, K., Ciftci, H.I., Kamo, M., Tateishi, H., Otsuka, M., and Fujita, M. (2017). Zinc-binding site of human immunodeficiency virus 2 Vpx prevents instability and dysfunction of the protein. The Journal of general virology *98*, 275-283.

Zhao, Y., Chapman, D.A., and Jones, I.M. (2003). Improving baculovirus recombination. Nucleic acids research *31*, E6-6.

Zheng, S.Q., Palovcak, E., Armache, J.P., Verba, K.A., Cheng, Y., and Agard, D.A. (2017). MotionCor2: anisotropic correction of beam-induced motion for improved cryo-electron microscopy. Nat Methods *14*, 331-332.

Zimmerman, E.S., Schulman, B.A., and Zheng, N. (2010). Structural assembly of cullin-RING ubiquitin ligase complexes. Current opinion in structural biology *20*, 714-721.

Zimmermann, A., Trilling, M., Wagner, M., Wilborn, M., Bubic, I., Jonjic, S., Koszinowski, U., and Hengel, H. (2005). A cytomegaloviral protein reveals a dual role for STAT2 in IFN-{gamma} signaling and antiviral responses. The Journal of experimental medicine *201*, 1543-1553.

Zivanov, J., Nakane, T., Forsberg, B.O., Kimanius, D., Hagen, W.J., Lindahl, E., and Scheres, S.H. (2018). New tools for automated high-resolution cryo-EM structure determination in RELION-3. Elife *7*.